AFGL-TR-77-0201

MODELING FOR MULTISPECTRAL INFRARED AND MICROWAVE REMOTE SENSING OF THE TROPOSPHERE

Paul A. Davis
John S. Osborn

SRI International
333 Ravenswood Avenue
Menlo Park, California 94025

September 1977

Final Report
15 August 1976—30 September 1977

This research was supported by the Air Force In-House Laboratory Independent Research Fund

UNCLASSIFIED

SECURITY CLASSIFICATION OF THIS PAGE (When Data Entered)

REPORT DOCUMENTATION PAGE

READ INSTRUCTIONS BEFORE COMPLETING FORM

1. REPORT NUMBER: AFGL-TR-77-0201
2. GOVT ACCESSION NO.
3. RECIPIENT'S CATALOG NUMBER

4. TITLE (and Subtitle)

MODELING FOR MULTISPECTRAL INFRARED AND MICROWAVE REMOTE SENSING OF THE TROPOSPHERE

5. TYPE OF REPORT & PERIOD COVERED

Final Report, 16 Aug 76 - 30 Sep 77
Covering the period 16 Aug 1976 - 30 Sept 1977

6. PERFORMING ORG. REPORT NUMBER

SRI Project ERU 5677

7. AUTHOR(s)

Paul A. Davis John S. Ostrem

8. CONTRACT OR GRANT NUMBER(s)

F19628-76-C-0275

9. PERFORMING ORGANIZATION NAME AND ADDRESS

SRI International
333 Ravenswood Avenue
Menlo Park, California 94025

10. PROGRAM ELEMENT, PROJECT, TASK AREA & WORK UNIT NUMBERS

ILIR6HAA

11. CONTROLLING OFFICE NAME AND ADDRESS

Air Force Geophysics Laboratory
Hanscom Air Force Base, Mass. 01731
Monitor/James T. Bunting/LYS

12. REPORT DATE: Sep 77
13. NO. OF PAGES: 88

14. MONITORING AGENCY NAME & ADDRESS (if diff. from Controlling Office)

15. SECURITY CLASS. (of this report)

UNCLASSIFIED

15a. DECLASSIFICATION/DOWNGRADING SCHEDULE

16. DISTRIBUTION STATEMENT (of this report)

Approved for public release; distribution unlimited

17. DISTRIBUTION STATEMENT (of the abstract entered in Block 20, if different from report)

18. SUPPLEMENTARY NOTES

This research was supported by the Air Force In-House Laboratory Independent Research Fund

19. KEY WORDS (Continue on reverse side if necessary and identify by block number)

Infrared Radiation
Microwave Radiation
Absorption Coefficients
Transmittance Modeling
Satellite Radiometric Measurements
Cloud Sensing
Satellite Meteorology
Remote Sensing Background

20. ABSTRACT (Continue on reverse side if necessary and identify by block number)

The major objective of this study was to establish background information on the relative responsiveness of multispectral infrared and microwave sensors typical of satellite radiometric sounders that probe tropospheric regions containing clouds. Such information supports satellite techniques to improve sensing of atmospheric structure and cloud features, and reduces the dependence on increased surface and airborne instrumentation. Different spectral intervals with the same equivalent temperature response from the cloud-free atmosphere also facilitate the interpretation of remote measurements in the presence of clouds or other aerosols.

DD FORM 1 JAN 73 1473
EDITION OF 1 NOV 65 IS OBSOLETE

UNCLASSIFIED

SECURITY CLASSIFICATION OF THIS PAGE (When Data Entered)

410 281

19. KEY WORDS (Continued)

20 ABSTRACT (Continued)

Extensive files of monochromatic absorption coefficients were generated at several pressures and temperatures; corresponding transmittances over uniform paths were computed, averaged, and modeled in a transmittance function with a universal representation in terms of conventional atmospheric variables. Numerous transmittance weighting functions were computed for interspectral comparisons. Tabulations of computed radiances and equivalent temperatures documented the variations due to changes in spectral interval, atmospheric structure, zenith angle, lower boundary height, and (for microwave radiances) surface emissivity and reflectance. Spectral regions examined included 400 cm^{-1} to 2500 cm^{-1} of the infrared and the 60 GHz oxygen, 22 GHz, and 183 GHz water vapor regions of the microwave spectrum.

Responses from some separated spectral intervals may be weighted to yield radiances with the same equivalent temperature when viewing a horizontally homogeneous atmosphere and background. However, over a horizontally inhomogeneous background the temperature response at the higher wave number will be largest because of the greater temperature sensitivity of the Planck function with wave number. The identification of widely separated spectral intervals that are matched in response is complicated both by the varying combinations of absorber types under different atmospheric conditions and by the spectral variation of the continuum. Perhaps the greatest potential for sensing in separated intervals with matched atmospheric response would be in the recognition of characteristic spectral variations due to specific radiative properties of various types of clouds.

Infrared radiance tabulations for pairs of intervals may be manipulated by using various lower boundary heights to extract general information relating to gross cloud features of amount and height. The infrared sensors (generally for 20 cm^{-1} intervals in this study) were relatively unresponsive to small temperature changes near the earth's surface but were well suited for the detection of changes induced by high clouds. In the microwave regions near 55 GHz (oxygen) and 183 GHz (water vapor) flexibility is allowed for the selection of frequencies at which to probe through various thicknesses of the atmosphere, although the response functions for the oxygen frequencies are broad. Computed brightness temperatures and their limb variations over lower boundaries with reduced emissivities show a dependence on the type of reflectance (specular or diffuse) assumed for the surface. Less limb brightening or enhanced limb darkening occurs over diffuse surfaces. In the weakly absorbing regions between about 19 and 37 GHz, it was found necessary to include both oxygen and water vapor in the modeling.

CONTENTS

ILLUSTRATIONS

ILLUSTRATIONS (Continued)

TABLES

I INTRODUCTION

The retrieval and interpretation of information from remote sensing of the real nonhomogeneous atmosphere requires a combination of accurate radiometric measurements and reliable computations of compatible atmospheric transmittances. For repetitive applications, it is not practicable to perform complete, rigorous computations of actual atmospheric transmittances on the basis of the characteristics of all absorption lines at all distributions of absorber amounts, pressures, and temperatures. However, it is practicable to design simplified, comprehensive transmittance representations that are based on transmittances computed rigorously for select idealized conditions. Once such flexible representations are achieved, they provide the basis both for the interpretation of measurements and for an a priori simulation of multispectral measurements. The simulation capability is particularly important for an experimental design involving passive multispectral radiometric probing as a means for acquiring information.

To be useful, a numerical model must agree reasonably well with observations of the actual atmosphere. Unfortunately, some of the atmospheric targets (e.g., clouds) for which information is desired through remote sensing impose difficulties in data interpretation because of uncertainties in their particulate distributions and radiative properties. Therefore, a logical first step in the development of tools for infrared remote sensing studies is the design of a suitable transmittance-radiance model for the molecular (clear) atmosphere. Such a model enables the description of clear-sky background radiances and permits inferences of the effects of clouds and other aerosols on radiance measurements from comparisons between measurements and computations. As more information becomes available, the transmittance model can be altered to include particulate constituents of the atmosphere.

Practical methods for defining multispectral transmittance representations for arbitrary absorber-pressure-temperature configurations were developed in previous studies,[1]* and form a basis for this study.

*References are listed at the end of the report.

II OBJECTIVES

The major objective of this study was the establishment of the basis for examining the relative responsiveness of multispectral infrared and microwave satellite sensors that can be applied for probing of that portion of the atmosphere (troposphere) that contains clouds. Multispectral measurements are often used to generate information regarding depth distribution of temperature or absorbers within the atmosphere. At distinctly different spectral regions the radiative properties of a target of interest (e.g., cloud) may vary significantly. Exploitation of the latter characteristics might best be accomplished by remote sensing in widely separated wavenumber intervals that offer the same response to the cloud-free atmosphere. Accordingly, this study emphasized examination of transmittance weighting function profiles for spectral regions responding to the middle and lower troposphere and typical of current satellite sounder instruments. The range of spectral regions considered extended from the near-infrared (4 μm) through several window regions and bands of carbon dioxide and water vapor into the rotational band of water vapor and out to the 60-GHz region of oxygen absorption, as well as the 183-GHz and 22-GHz lines of water vapor.

From the point of view of cloud probing potential, responsiveness to the lower troposphere is important. The broad nature of typical response (weighting) functions means that emission from the lower boundary is included in the response. Therefore, any background study such as this must include variations in the lower boundary as well as those of the atmosphere. Typical atmospheric variations that influence the response include temperature-moisture structural changes and changes in viewing angle. Of course, cloudiness itself would change with view angle.

The effects of clouds on the radiometric response can only be examined properly with adequate radiation models of the clouds themselves. However, in addition to background response variations, some gross cloud effects can be estimated from data summaries compiled in this study.

III APPROACH

Figure 1 is a summary of the major tasks undertaken to meet the objectives discussed above. Some of the pertinent details of each step will be discussed in later sections. Both microwave and infrared radiation are included in each study phase. A summary of computer programs used in this study is presented in Appendix A.

Since subsequent transmittance models for spectral bands should be consistent with line-by-line calculations for any prescribed response function, it is necessary to base the modeling on the individual absorption line parameters (position, strength, half-width, and energy of the lower state). The initial, and most costly, study phase is the use of the absorption line parameters in conjunction with a suitable line shape to generate detailed files of monochromatic absorption coefficients at a variety of pressures and temperatures characteristic of the atmosphere. All pertinent molecular absorbers in the atmosphere must be included in the computations. The maximum spectral spacing for the computations is governed by the line shape and the pressure-dependent half-width at half-maximum. In addition to the transmittance model input, computed absorption coefficients can assist in the selection of spectral intervals of particular interest or in the evaluation of relative performance of numerical transmittance models.

The next major step is the infrared transmittance modeling itself. This begins with the calculation of monochromatic transmittances from the calculated absorption coefficients. A tremendous data compression is then obtained by averaging the transmittances over specified spectral intervals of interest. During the averaging, any prescribed spectral response function can be convolved with the monochromatic transmittances. Next, a selected one-parameter transmittance function that incorporates the averaged transmittance is evaluated for each absorber-pressure-temperature combination simultaneously with a two-parameter representation

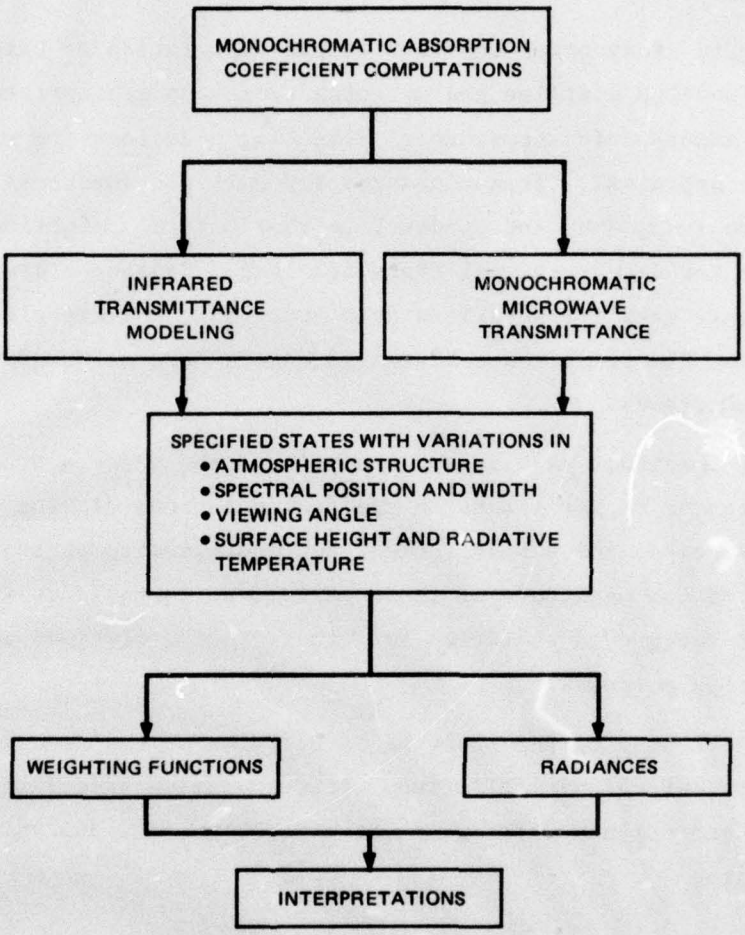

FIGURE 1 ORGANIZATION OF STUDY PHASES

of the transmittance function solely in terms of the atmospheric variables. The latter representation is generalized to include temperature-dependent scaling coefficients that cause all data points to cluster along a single curve. Microwave transmittances are not modeled in the same way; only monochromatic microwave transmittances are computed in direct applications for this study.

The third study phase consists of the calculation of transmittance weighting function profiles and outgoing radiances appropriate to actual prescribed atmospheric structures. Weighting functions are graphed for interactive appraisal. Transmittances for multiple absorbers in a given interval are treated as independent, so that a total weighting function is based on the product of all transmittances. Radiances are compiled in units commonly used for satellite data archiving, and are also converted to equivalent Planckian temperatures to enable more meaningful inter-channel comparisons.

A most important task is the analysis of the effects on the satellite-sensed radiances of variations in spectral position, viewing angle, atmospheric structure, and surface height and radiative temperature. The documentation of the magnitude of these variations in radiance is useful for analyses of background radiation for other probing missions and for planning or design purposes.

The final step of the study is an overview of the numerical results depicting background variabilities. Interpretative speculations or estimations of gross cloud effects can be made by special analysis of tabulated results.

IV ABSORPTION COEFFICIENTS

A. Infrared

All of the infrared absorption line parameters (with the exception of line shape) required for the detailed computation of absorption coefficients were taken from the AFGL compilations stored on magnetic tape.[2] A program labeled RDGOAT was written to read the AFGL tape, extract the line parameters [strength (S), resonant position (ν_o), half-width (γ_o) and energy of the lower state (E″)] for the particular absorbers and spectral regions of interest. Extracted data were printed and stored on another tape. Ratios of Lorentz to Doppler line widths were compiled at two temperatures and included in the listing. These ratios could be used if required in approximation methods for computing absorption coefficients for Voigt line shapes (cf Kielkopf[3]), given the results for Lorentz line shapes.

For this investigation, which was confined to troposphere influences, it was considered adequate to use only the Lorentz line shape even though the weighting function for some intervals extended into the stratosphere. Thus the absorption coefficient is given by

$$k(\nu) = S\gamma/\pi\left[(\nu - \nu_o)^2 + \gamma^2\right] \quad . \tag{1}$$

The pressure (P) and temperature (T) dependence of the half-width can be described by

$$\gamma = \gamma_o(P/P_o)\ (T_o/T)^n \tag{2}$$

where the exponent n is usually taken as 0.5 or 0.62, depending on the absorber and type of broadening. The temperature dependence of the line strength can be approximated with

$$S = \{S_o\ Q_v(T_o)\ Q_r(T_o)/[Q_v(T)\ Q_r\ (T)]\}\ \exp\ [1.439\ E''(T-T_o)/T\ T_o] \tag{3}$$

where the vibrational and rotational transition functions also have been approximated by

$$Q_v(T) = a + bT + cT^2 \tag{4a}$$

$$Q_r(T) = (T/T_o)^j \quad . \tag{4b}$$

The exponent j is 1.5 for H_2O, O_3, and CH_4; for other absorbers in this study, j is unity. The constant a is assigned the value unity while b and c are taken as zero with the exceptions defined in Table 1.

Table 1

CONSTANTS USED IN APPROXIMATION OF
TEMPERATURE DEPENDENCE OF LINE STRENGTHS
(see Eqs. 4 in text)

Molecule	a	b	c
CO_2	1.05453	-8.173E-04	3.20E-06
O_3	1.06283	-7.422E-04	2.31E-06
N_2O	1.056	-8.911E-04	3.82E-06

Given the absorber and the wavenumber, only the pressure and temperature must now be specified for a computation of absorption coefficient. To be compatible with files of absorption coefficients generated previously, computations were made for three temperatures (300, 250, and 200 K) and four pressures (0.9, 0.5, 0.2, and 0.06 atm for H_2O; 0.9, 0.3, 0.09, and 0.03 atm for uniformly mixed gases; 0.9, 0.25, 0.08, and 0.025 atm for O_3). At each computational position, contributions from lines within $\pm$ 10 cm^{-1} were included. The spacing between wavenumbers at which the monochromatic absorption coefficients were compiled was varied from $.05^{-1}$ at the highest pressure to .004 cm^{-1} at lower pressures (still with Lorentz line shape).

When combined with previous absorption coefficient computations, all significant absorption between 20 cm^{-1} and 2560 cm^{-1} has been covered with one major exception: the ozone absorption bands between about 990 and 1110 cm^{-1}. Inasmuch as the principal ozone absorption occurs at altitudes above the clouds, this spectral region, with a very large number of lines, was excluded for reasons of economy. Absorption lines also were ignored in adjacent regions dominated by the water vapor continuum.

Absorption coefficients were generated for a wide variety of intervals and absorbers; a number of spectral gaps from previous work were filled. In addition to H_2O, CO_2, and some O_3 bands, other absorbers included N_2O, CO, and CH_4. The latter three gases were assumed to be uniformly mixed, as was CO_2. Consequently, it was possible to condense the absorption coefficients in regions where more than one of the uniformly mixed gases was active. If each absorption coefficient is multiplied (weighted) by the ratio of its mixing ratio to that for CO_2, then the weighted sum of the combined absorption coefficients can be treated as the new absorption coefficient for an equivalent concentration of CO_2. If each of the mixing ratios is denoted by r, then, for example,

$$r_{CO_2} k_{CO_2} + r_{CO} k_{CO} + r_{N_2O} k_{N_2O} = r_{CO_2} \left(k_{CO_2} + \frac{r_{CO}}{r_{CO_2}} k_{CO} + \frac{r_{N_2O}}{r_{CO_2}} k_{N_2O} \right)$$

$$= r_{CO_2} k_{UMG} \qquad (5)$$

where the single combination absorption coefficient (UMG denotes Uniformly Mixed Gas) is applied only to equivalent amounts of carbon dioxide along the path.

Figure 2 illustrates a resultant UMG absorption coefficient distribution that originates from a combination of CO_2 and N_2O absorption coefficients. It is apparent that the CO_2 distribution is very similar to the final UMG distribution, despite the greater magnitude of the absorption coefficients for N_2O. The reason for this is that the N_2O mixing ratio in the atmosphere is three orders of magnitude less than that of

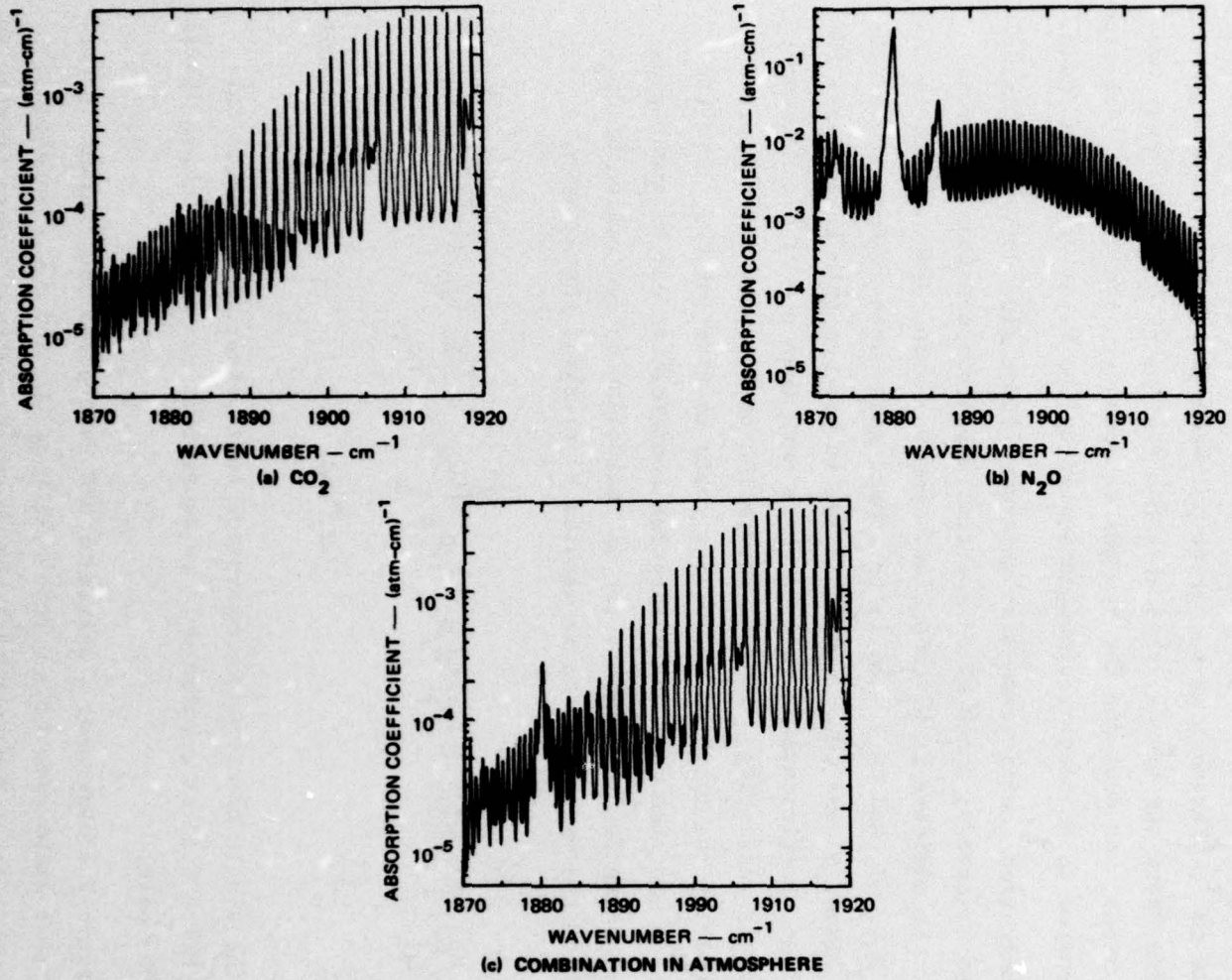

FIGURE 2 ABSORPTION COEFFICIENTS FOR INDIVIDUAL GASES AND THEIR UNIFORMLY MIXED ATMOSPHERIC COMBINATION (TEMPERATURE = 300 K, PRESSURE = 0.9 atm)

CO_2. Only the stronger lines of N_2O below about 1890 cm^{-1} have an influence on the UMG curve; easiest to detect are lines near 1872, 1880, and 1886 cm^{-1}.

Absorption coefficients for the water vapor continuum and the nitrogen-induced continuum in this study have been taken directly from the LOWTRAN 3B model of Selby et al.[4] Extensions of coefficients (for both self and foreign gas broadening and their temperature-dependent coefficients) out to 325 cm^{-1} within the rotational band of H_2O were made possible by preliminary information.* Adjustments appearing in LOWTRAN 3B are discussed primarily by Roberts et al.[5]

B. Microwave

Whereas the monochromatic absorption coefficients computed for absorbers in the infrared were used in modeling over intervals as large as 20 cm^{-1}, the absorption coefficients for the microwave were both computed and applied monochromatically. Thus, for the microwave region no files of absorption coefficients were prepared and stored; each coefficient is computed as needed in application.

The absorption coefficient throughout the 5 mm oxygen band was based entirely on the treatment presented by Rosenkranz[6] with very useful approximations for dealing with the theory of overlapping lines. The absorption coefficient $k(\nu)$ may be expressed by

$$k(\nu) = CP(\nu/T)^2 F \tag{6}$$

where C is a constant. The shape function F may be described by

$$F = P\left\{\sum_N \Phi_N \left[f_N^+(\nu) + f_N^+(-\nu) + f_N^-(\nu) + f_N^-(-\nu)\right] + .7w_b/\left(\nu^2 + P^2 w_b^2\right)\right\} \tag{7}$$

where Φ_N is the fractional population of the initial state associated with rotational quantum number N, and the summation (over odd values of

*Courtesy of Dr. Robert M. McClatchey, AFGL

N) of the shape function factors f covers all branches of significant lines (including those at negative symmetric frequencies) contributing to resonant absorption. The last term represents the nonresonant contribution, with w_b representing nonresonant half-width per unit pressure. Other near-diagonal elements (w) of the transition rate matrix, frequencies and amplitudes of oxygen lines, and interference coefficients are all provided in tabular form by Rosenkranz; each of the shape function factors is defined in terms of these data. Temperature dependence enters through the fractional population Φ_N and through the resonant and nonresonant line half-widths.

For water vapor at the microwave frequencies, the absorption coefficient was computed using two different approaches and two line shapes. One expression for the absorption coefficient was discussed by Staelin;[7] the other approach was described by Gaut and Reifenstein.[8] The Staelin and Gaut expressions, respectively, for the monochromatic absorption coefficient (used here in terms of nepers km^{-1}) can be put in the forms

$$\sigma(\nu) = \left(\rho_w/T^{2.5}\right)\nu^2\Delta\nu\left[C_1 e^{-c/T_F} + C_2 T\right] \tag{8a}$$

and

$$\sigma(\nu) = \left(\rho_w/T^{2.5}\right)\nu^2\left[\Delta\nu C_1 e^{-c/T_F} + C_2 P T^{1-n}\right] \tag{8b}$$

where $\Delta\nu = C_3\ (P/T^n)(1 + C_4\rho_w T/P)$ and the constants C_1, C_2, C_3, and C_4 differ with model and resonant frequency. F is the line shape factor,

$$F = \frac{1}{(\nu-\nu_o)^2 + \Delta\nu^2} + \frac{1}{(\nu+\nu_o)^2 + \Delta\nu^2}$$

for the Van Vleck-Weisskopf shape, ρ_w is the water vapor density, c includes the energy of the initial state, and $\Delta\nu$ is the appropriate line half-width. With the Gaut model and the resonant frequency of

ν_o = 22.235 GHz, the constants c = 642, C_1 = 358, C_2 = .0002, C_3 = .0984, C_4 = .01978, and n = .626. For ν_o = 183.31 GHz the constants c = 196, C_1 = 221, C_2 = .000228, C_3 = .1196, C_4 = .01906, and n = .649.

V INFRARED TRANSMITTANCE MODELING

The computed monochromatic absorption coefficients for pertinent gases at realistic ranges of pressure and temperature form the basis for transmittance modeling. The modeling procedure is the same as that applied previously.[1]* Fundamentally, the transmittance model sought is a simple formulation (involving a minimum of parameterization) that would be expressable explicitly in terms of atmospheric variables and should provide a sufficiently universal fit, regardless of temperature or pressure, that all points follow a single curve. If a good-enough fit is achieved, then it is possible to replace the nonhomogeneous path with an equivalent homogeneous path. Previous experience with the model technique suggested that the best results might be obtained for spectral intervals of about 15 cm^{-1} or greater.

To begin the transmittance modeling (see Figure 3) spectral intervals must be selected and a meaningful set of absorber amounts must be provided for association with the absorption coefficients. In practice, five different absorber amounts were assigned to each of four pressures at each of three temperatures. The amounts were selected to conform to realistic encounters over atmospheric paths. If the absorption was too weak, the amounts would be increased to provide sufficient data samples for the computational phases.

The first computational step is to compute all of the monochromatic transmittances associated with absorption coefficient k_ν and absorber amount W:

$$\tau_\nu = \exp\left[-k_\nu(P,T)\, W\right] \quad . \tag{10}$$

---

*Previous results could not be used here because they were designed for specific instrument response functions.

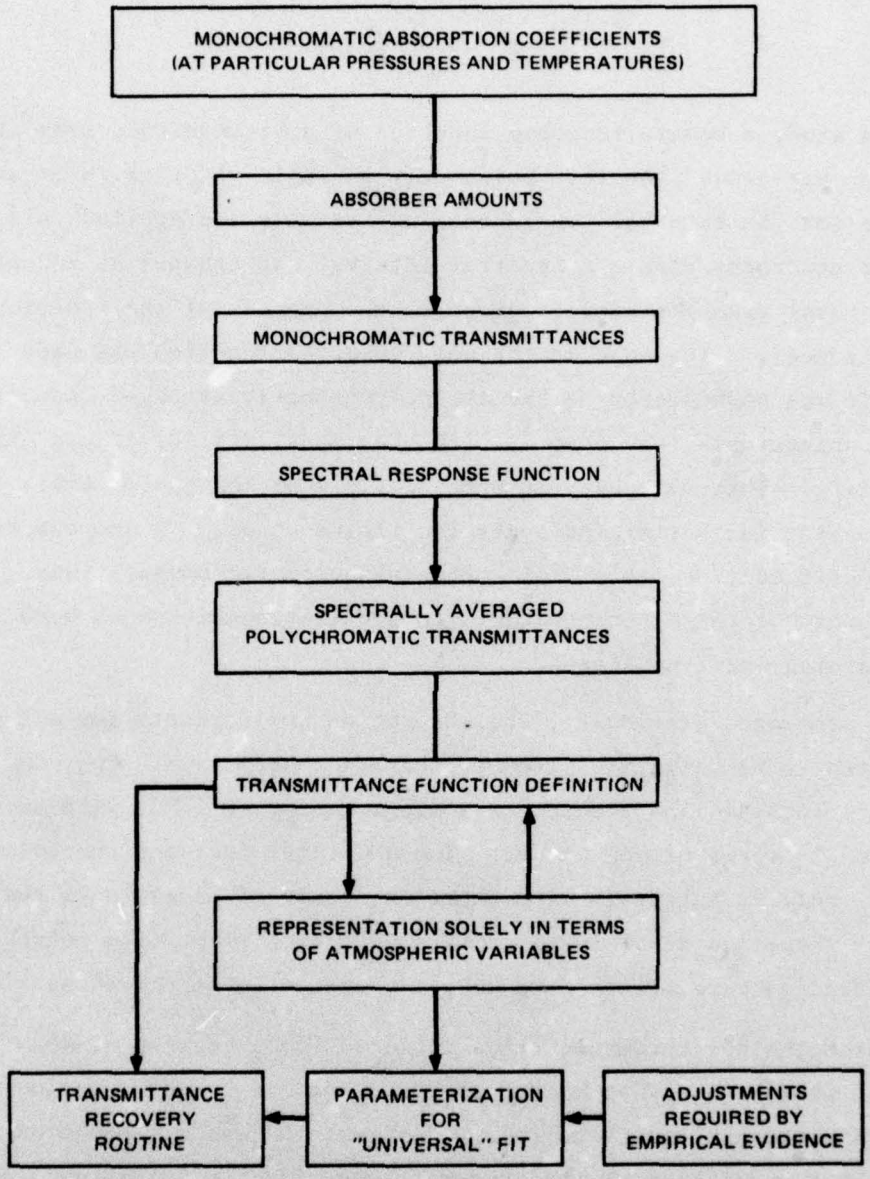

FIGURE 3 INFRARED TRANSMITTANCE MODELING PROCEDURE

The many monochromatic transmittances, after convolution with a spectral response function ω_ν, are compressed by several orders of magnitude through the integration over the given spectral interval $\Delta\nu$

$$\tau_{\Delta\nu} = \int \tau_\nu \omega_\nu \, d\nu \Big/ \int \omega_\nu d\nu \quad . \tag{11}$$

For this study a square response function of unit magnitude over the interval $\Delta\nu$ was used. [At this point only a single absorber is treated at one time for the interval $\Delta\nu$. When final results are applied, all significant absorbers within a spectral interval are treated as independent, and the total transmittance is given as the product of the individual transmittances.] Inasmuch as the unit response function was used in this study, it was possible to define the polychromatic averaged transmittances within subintervals (say 5 cm^{-1}) with the capability for simple extension to any larger interval that was some multiple of the subinterval. Accordingly, an initial set of intervals (multiples of 5 cm^{-1}) and absorbers were identified (see Table 2) for the polychromatic computations. It was from subsets of these data that polychromatic transmittances were input to the remaining modeling stages.

As mentioned previously, the absorption coefficients for all gases considered to be uniformly mixed in the atmosphere (e.g., CO_2, CO, CH_4, N_2O) were combined and treated as a single absorber (UMG) with amounts specified in terms of CO_2 amount. The UMG label included the intervals with CO_2 only or intervals with other uniformly mixed gases in the absence of CO_2. Thus, the final infrared absorbers with identified polychromatic transmittances were either H_2O, UMG, O_3, or continuum (discussed later).

Given the polychromatic transmittances for a variety of absorber amounts, pressures, and temperatures, the next step was to define a suitable transmittance function (i.e., some function which depends only on τ). Given the transmittance τ, the transmittance function takes on a numerical value; on the other hand, given the value of the transmittance function, the transmittance can be recovered. An example of a transmittance function might be $\log_e \tau$, or $\log_e(-\log_e \tau)$. Such simple transmittance functions sel-

Table 2

SPECTRAL INTERVALS AND ABSORBERS CONSIDERED IN POLYCHROMATIC TRANSMITTANCE COMPUTATIONS

Spectral Range (cm^{-1})	Absorbers[+]
* 340 - 380	H_2O
440 - 470	H_2O
530 - 560	H_2O, (CO_3), (N_2O)
* 680 - 720	H_2O, CO_2, O_3
720 - 760	H_2O, CO_2, O_3
880 - 900	Continuum
1190 - 1210	Continuum
*1240 - 1270	H_2O, N_2O, CH_4
1360 - 1390	H_2O, (CH_4)
*1550 - 1570	H_2O
*1680 - 1700	H_2O
1920 - 1950	H_2O, (CO_2)
*2000 - 2030	H_2O, (CO_2), (CO)
2060 - 2090	H_2O, CO_2, O_3
2090 - 2120	H_2O, CO_2, O_3
2170 - 2200	H_2O, CO_2, N_2O, CO
2230 - 2260	H_2O, CO_2, N_2O, CO
*2280 - 2310	(H_2O), CO_2, (N_2O)
2500 - 2520	Continuum

*Subsequently dropped from further analysis to reduce scope.

[+]Absorbers in parentheses not actually used in modeling. Continuum considered over entire spectral range.

dom would apply to all ranges of absorber-pressure-temperature combinations without introduction of a series of parameters. The form adopted here for transmittance function ψ_c is the same as that used and discussed previously:

$$\psi_c = \left[C \frac{2}{\sqrt{\pi}} \Phi^{-1}(1 - \tau)\right] + (1 - C)\left[-\log_e \tau\right] \quad . \tag{12}$$

This two-term form with the parameter C, where Φ^{-1} is the inverse error function with argument $(1 - \tau)$, is characteristic of a combination of regular and random transmission models, blended in accordance with the magnitude of C. With C = 0 the random model prevails whereas with C = 1 the regular model prevails. For almost all situations encountered, the value of C ranges between 1.0 and -1.0, but occasionally extends to -2.0 with a good representation. When the best fitting C was less than -2.0, the sensitivity to C was very slight or the transmittances did not fit well to a single curve. Although not encountered in practice, a limitation of Eq. (12) exists on physical grounds since ψ_c must be positive. For very small τ this function could become negative for C greater than unity; if five places are retained in τ and if τ = .00001, then C cannot exceed 1.39 for ψ_c to remain positive. Even that occurrence could be prevented by the addition of a suitable correction term including C, 1 - C, and the difference between $\ell n\ \tau$ and $\frac{2}{\sqrt{\pi}} \Phi^{-1}(1-\tau)$ as factors (not required in the present application).

The numerical technique for recovering the transmittance τ from the transmittance function (Eq. 12) is given in Appendix B. What has not been discussed is the manner in which the parameter C is determined. A key step in the modeling procedure is to solve for C simultaneously with the parameters of a representation of the transmittance function solely in terms of atmospheric variables. The form adopted* for the atmospheric representation,

$$\psi_c = A_T W \Big/ \sqrt{(W/P) + B_T^2} \tag{13}$$

---

*In a previous study the right hand side of Eq. (13) was slightly more complicated with an additional appearance of B_T in the denominator

$$\psi_c = A_T W \Big/ \left(\sqrt{(W/P) + B_T^2} + B_T\right) \quad .$$

For C=0 this form corresponds with the Malkmas[9] model whereas Eq. (13) corresponds with the Goody[10] model.

contains two temperature-dependent parameters, A_T and B_T. In practice, with C expressed according to Eq. 12, transmittances are introduced for the reference temperature T_0 (250 K). The equations are solved by a nonlinear least-squares technique to determine the best fitting A_0, B_0, and C in terms of a dependent and two independent variables. Table 3 contains a listing of these constants for the noncontinuum regions of Table 2. The value of C so determined is taken as a constant independent of temperature (an approximation). Now the left side of Eq. (13) is fully defined, so that the nonlinear least-squares curve-fitting technique can be reapplied to obtain the best fitting parameters A_T and B_T at each of the three temperatures considered in the modeling. For some regions the best fit is obtained with the single parameter A_T (i.e., let $B_T = 0$):

$$\psi_c = A_T \sqrt{WP} \quad . \tag{14}$$

The solution of A_T and B_T from Eq. (13) or A_T from Eq. (14) has resulted in excellent representations of data points at all pressures and absorber amounts by a single curve for a given temperature. However, with C held fixed on the left side, the parameters A_T and B_T for the three temperatures can be used to define temperature-dependent scaling coefficients for the independent variables, in terms of a second-degree polynomial in temperature. Suppose the scaled independent variables in Eqs. (13) and (14) are defined as

$$(W^*) = \int S_1(T)\, dW \tag{15a}$$

$$(WP)^* = \int S_2(T)\, P\, dW \tag{15b}$$

$$(W/P)^* = (W^*)^2 \,/\, (WP)^* = \left[\int S_3(T)/P\, dW\right]^{\dagger} \tag{15c}$$

---

†Not required as separate specification since $S_3(T) = [S_1(T)]^2 \,/\, S_2(T)$.

Table 3

INITIAL PARAMETERS AT DEFINED REFERENCE TEMPERATURE FOR TRANSMITTANCE MODELING IN SELECTED 20 cm^{-1} INFRARED INTERVALS

Interval (cm^{-1})	A_0	B_0	C
Water Vapor			
440-460	2.854	--	0.199
445-465	2.020	--	0.514
450-470	1.992	--	0.635
530-550	0.762	--	0.747
535-555	0.912	--	0.745
540-560	0.961	--	0.257
1360-1380	3.088	--	0.817
1365-1385	2.403	--	0.826
1370-1390	2.856	--	0.697
1920-1940	0.908	--	0.607
1925-1945	0.894	--	0.626
1930-1950	1.248	--	0.273
680-700	0.334	-0.182	0.326
685-705	0.354	0.184	0.726
690-710	0.369	0.199	0.562
695-715	0.338	0.235	0.378
700-720	0.222	-0.256	0.175
705-725	0.206	-0.208	-1.469
710-730	0.118	0.506	-1.161
715-735	0.100	0.460	-0.587
720-740	0.093	-0.419	-0.364
725-745	0.176	-0.374	-0.350
730-750	0.162	-0.354	0.442
735-755	0.177	-0.384	0.286
740-760	0.181	-0.387	0.315
2060-2080	0.384	0.190	-0.043
2065-2085	0.219	0.181	0.844
2070-2090	0.198	0.396	1.029
2090-2110	0.182	0.337	0.517
2095-2115	0.166	0.532	0.463
2100-2120	0.157	0.440	0.180
2170-2190	0.077	1.142	0.461
2175-2195	0.066	1.397	0.516
2180-2200	0.064	1.377	0.391
2230-2250	0.066	3.420	-0.003
2235-2255	0.066	3.520	0.343
2240-2260	0.093	2.514	-0.922

Interval (cm^{-1})	A_0	B_0	C
Uniformly Mixed Gases			
680-700	0.068	0.523	0.552
685-705	0.522	0.644	0.528
690-710	0.380	0.860	0.502
695-715	0.268	1.235	0.531
700-720	0.228	2.075	0.494
720-740	0.164	2.547	-2.060
725-745	0.095	3.481	0.779
730-750	0.091	3.746	0.534
735-755	0.070	4.446	0.542
740-760	0.059	6.113	-0.089
2060-2080	0.031	10.444	0.0
2065-2085	0.028	10.983	0.0
2070-2090	0.023	10.643	0.0
2170-2190	0.044	17.524	0.516
2175-2195	0.053	11.756	0.454
2180-2200	0.070	9.523	0.389
2230-2250	0.240	4.230	0.679
2235-2255	0.235	3.200	0.792
2240-2260	0.230	1.906	0.886
Ozone			
680-700	0.954	5.764	-0.090
685-705	0.868	5.983	-0.299
690-710	0.767	5.664	-0.238
695-715	0.834	5.846	-0.190
700-720	0.955	5.499	-0.250
720-740	1.081	6.854	-0.539
725-745	0.971	7.578	-0.364
730-750	0.785	7.394	-0.410
735-755	0.742	7.485	-0.457
740-760	0.654	7.666	-0.307
2060-2080	0.502	3.762	-0.133
2065-2085	0.804	3.838	-0.329
2070-2090	1.066	3.416	-0.157
2090-2110	1.950	3.005	-0.278
2095-2115	1.850	3.221	0.490
2100-2120	2.067	3.298	-0.637

where

$$S_1(T) = (A_T B_o) \Big/ (A_o B_T) \cong 1 + a_1(T - T_o) + a_2(T-T_o)^2 \qquad (16a)$$

$$S_2(T) = A_T^2 \Big/ A_o^2 \cong 1 + a_3(T - T_o) + a_4(T - T_o)^2 \qquad (16b)$$

$$\left[S_3(T) = B_o^2 \Big/ B_T^2 \cong 1 + a_5(T - T_o) + a_6(T - T_o)^2\right]^{\dagger} \quad . \qquad (16c)$$

The coefficients in Eq. (16) are determined from information at the two nonreference temperatures. When the scaling coefficients are applied to the variables, all data points should fall on a single curve, rather than a separate curve for each temperature. When this is accomplished a "universal" representation has been achieved, in which the single curve,

$$\psi_c = A_o W^* \Big/ \sqrt{(W/P)^* + B_o^2} \qquad (17)$$

describes the transmittance regardless of absorber amount, pressure, or temperature. If such a universal curve has been achieved, then it has been demonstrated that a corresponding equivalent homogeneous path can replace the nonhomogeneous path. The explicit relationship to arbitrary distributions of atmospheric variables has great potential for generating matrices of coefficients that could be used in fast techniques[11, 12, 13] for extending transmittances through the atmosphere.

Although success has been achieved with the modeling technique described, that is not to say that the technique will always work anywhere or that adequate empirical tests have been made. In fact, for some spectral regions (not considered here) problems were experienced. A number of alternative forms to that expressed by Eq. (13) or (14) were tried, but generally met with less success. The lack of improvement persisted even with the addition of a single term and another parameter.

---

†See footnote on previous page.

Examples of the fits achieved by Eqs. (13) and (14) reveal how well the theoretical data can be modeled. In the illustrations, different symbols are maintained for the three different temperatures, but the various pressures and absorber amounts within each temperature category are not distinguished. Figure 4 illustrates the results obtained from Equation (14) for water vapor in the interval 530-550 cm. At the top, data points are plotted as computed, but the curve defined for standard temperature is shifted in accordance with the scaling factors for 300 K and 200 K. Each shifted curve and the reference curve (250 K) follow the distribution of points very closely. Similarly, when the universal curve at the reference temperature is plotted and data points are shifted in accordance with Equations (15) and (16), then a single curve with well clustered points is obtained, as shown in Figure 4b.

Similar results are obtained for water vapor in another spectral interval, 725-745 cm^{-1}, where the absorption is much weaker. In this region the two-parameter form of Equation (13) is superior. Figure 5a shows the excellent results from shifting the curves to meet the points and Figure 5b from scaling the points to coincide with the universal curve. It would be difficult to improve the fit. Figure 6a shows the fit of all data points (with temperature-dependent shifts applied) to the reference curve for ozone in the same spectral region. Here the data points occur in distinct clumps (determined by choice of conditions) as a result of the lack of any significant shifts with temperature, which normally would shift warmer points in one direction and colder points in the opposite direction. Figure 6b shows a similar plot for CO_2 for which more dispersion results from the temperature-dependent scaling. It may be noted that some points on one tail of the curve do not fit with the curve. This represents about the most serious departure observed in <u>any</u> of the fitted curves. The slight displacement probably is due to the Q branch near 741 cm^{-1} A plot of the CO_2 absorption coefficients for the spectral region is shown in Figure 7.

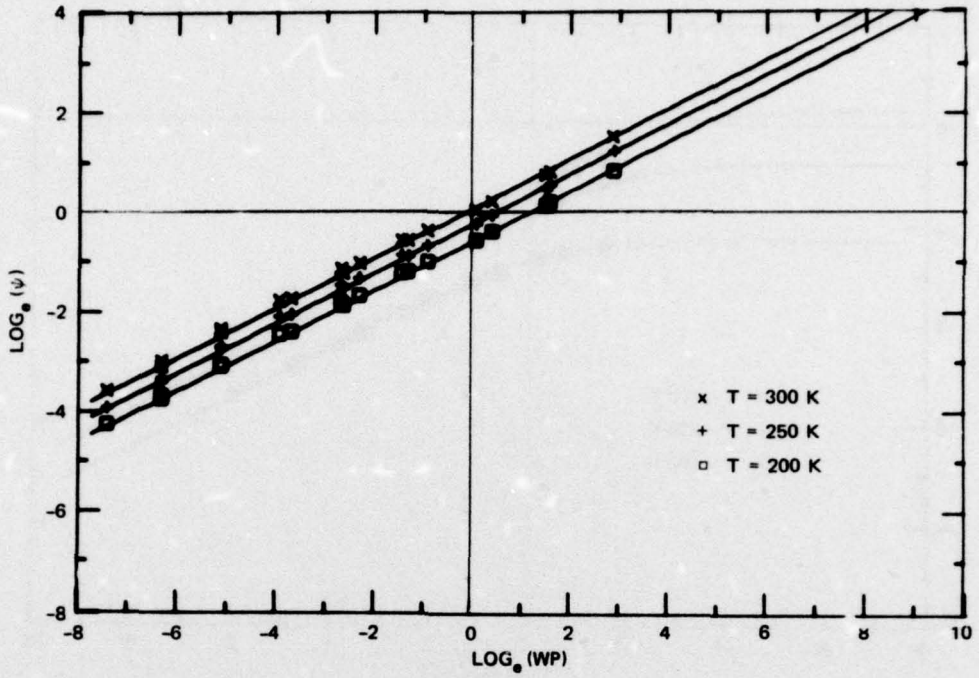

(a) CURVES SHIFTED

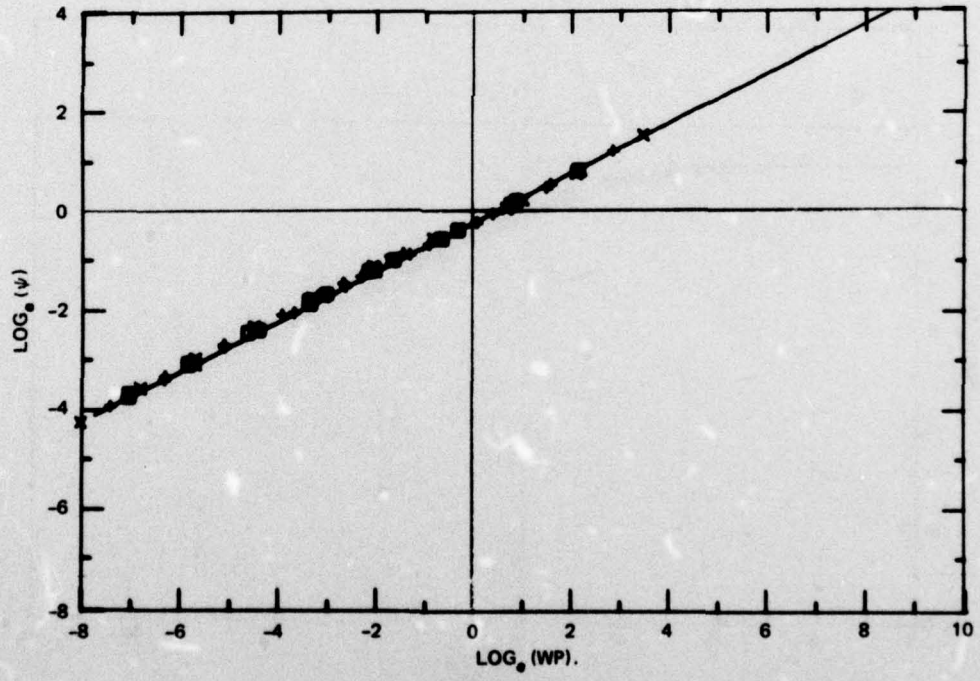

(b) DATA POINTS SCALED

FIGURE 4 UNIVERSAL REPRESENTATION OF WATER VAPOR TRANSMITTANCE, 530-550 cm^{-1} (FOUR PRESSURES, THREE TEMPERATURES)

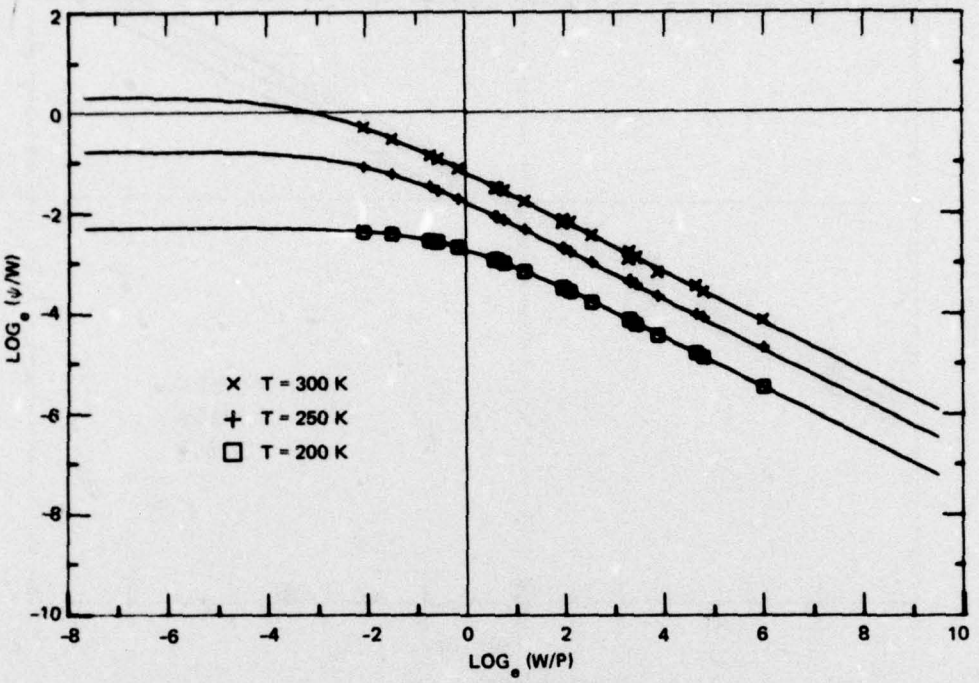

(a) CURVES SHIFTED

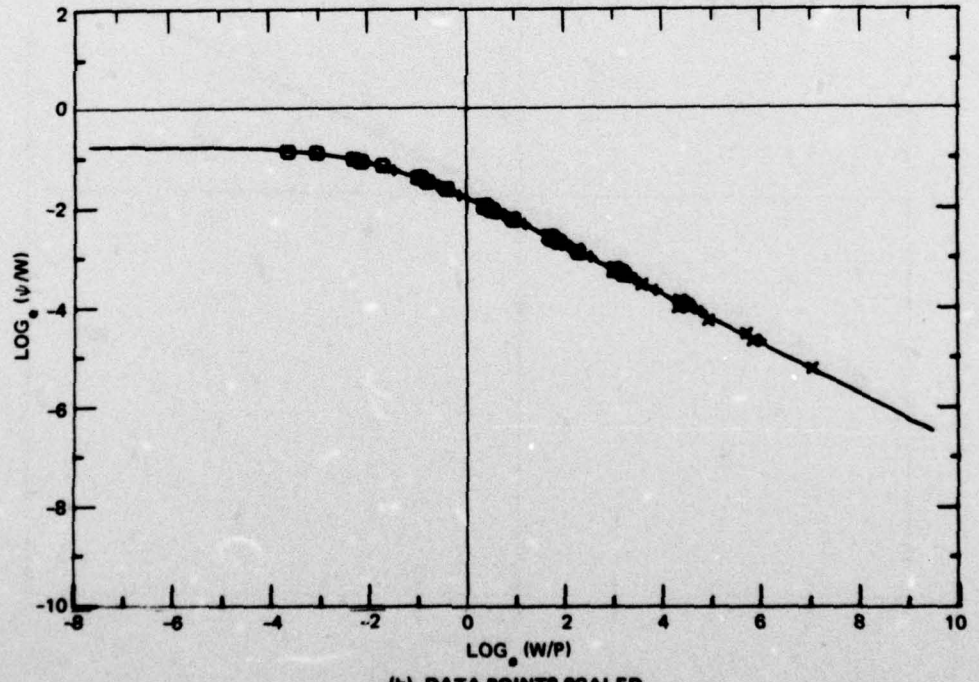

(b) DATA POINTS SCALED

FIGURE 5 UNIVERSAL REPRESENTATION OF WATER VAPOR TRANSMITTANCE, 725-7 cm^{-1} (FOUR PRESSURES, THREE TEMPERATURES)

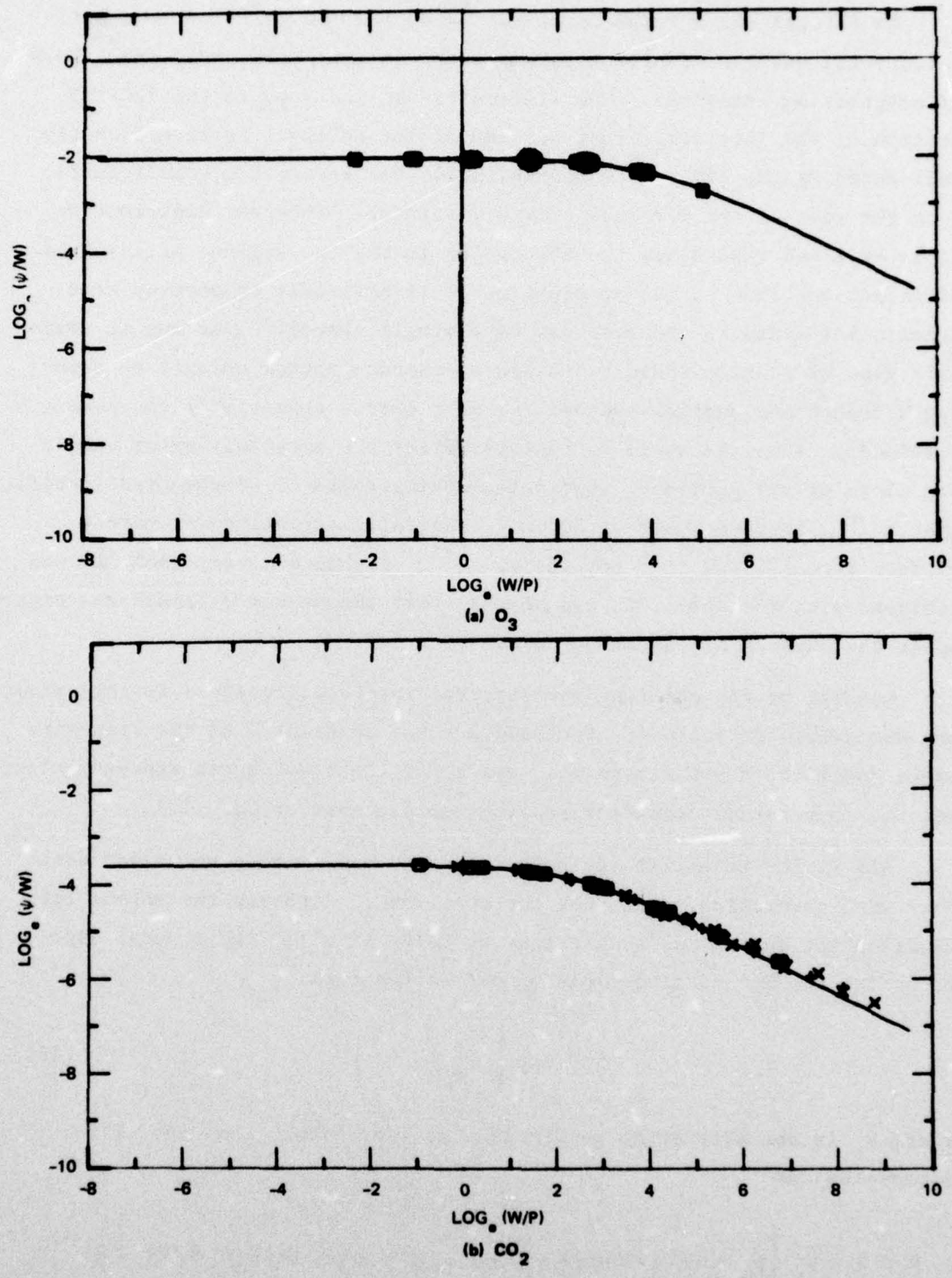

FIGURE 6 UNIVERSAL REPRESENTATIONS FOR OZONE AND CARBON DIOXIDE TRANSMITTANCES, 725-745 cm^{-1} (FOUR PRESSURES, THREE TEMPERATURES)

An initial fit for the spectral region 720-740 cm^{-1} led to a satisfactory fit but the resultant parameters were quite different from those of neighboring intervals. The difficulty was isolated to the 720-725 portion of the interval. That portion of the interval is significantly influenced by the 720 cm^{-1} Q branch, while the absorption coefficients over the rest of the interval show a distinctly different distribution. It is believed that since the absorption in the two regions arises from different portions of the atmosphere, it is difficult to portray atmospheric influence in the response of a single channel. One way to avoid this type of problem would be to use a separate narrow channel to cover the Q branch and another channel (or more narrow channels[14]) to cover the remainder. Thus, it would be best to select the intervals after examining plots of all pertinent absorption coefficients or of computed specific spectra.[15] In this study of 20 cm^{-1} intervals, attention was merely shifted from 720-740 cm^{-1} to 725-745 cm^{-1}. Although a very good fit was achieved with the shift, it can be seen that the weaker Q-branch was picked up at the expense of the strong one.

Results of the modeling for spectral intervals retained in this study are summarized in Table 4. Included are the constant C of the transmittance function, the parameters A_0 and B_0 of the atmospheric representation, and the temperature-dependent scaling coefficients of Eq. (17).

All of the transmittance modeling discussed to this point has dealt only with absorption lines--not the continuum. Although the method for handling the continuum is described by Selby et al.,[4] the general expressions for the H_2O continuum can be put in the form

$$\tau = \exp\left[-k_s \int U \, dz\right] \tag{18}$$

where k_s is the absorption coefficient at temperature 296K for self-broadening and

$$U = 0.1\, p_w \left\{ p_w \exp[C_2(296/T) - 1)] + C_3(P - p_w) \exp[C_4(296/T) - 1)] \right\} \tag{19}$$

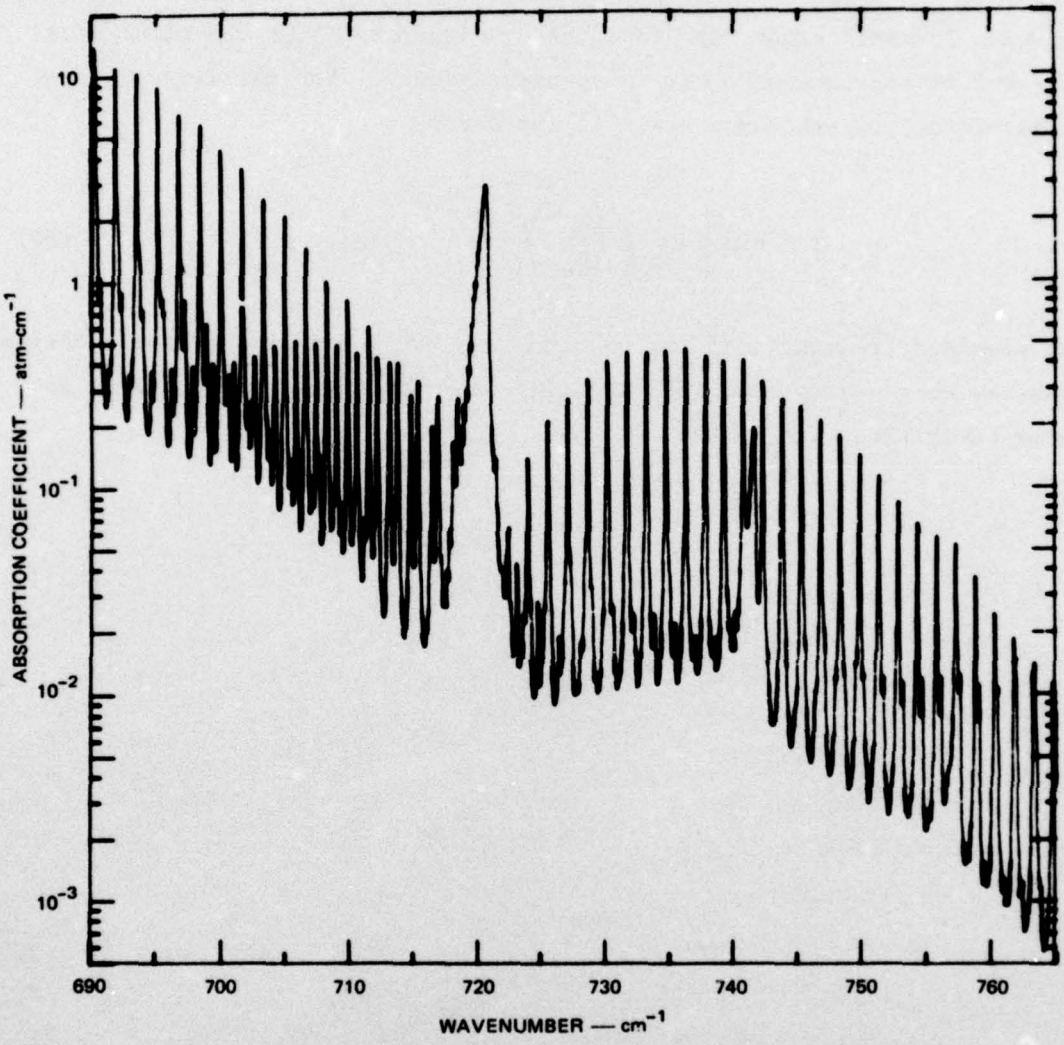

FIGURE 7 ABSORPTION COEFFICIENTS FOR CARBON DIOXIDE, 690-765 cm^{-1} (TEMPERATURE = 300 K, PRESSURE = 0.9 atm)

for ρ_w (water vapor density) in g m^{-3}, p_w (vapor pressure) and P (total pressure) in atm, and T (temperature) in Kelvins. The height z is taken in km. In application, the constant C_4 either takes on the value 0 or C_2, but it can take on other independent values. For the nitrogen continuum, the transmittance has been expressed as

$$\tau = \exp\left[-C_s \int \left(\frac{p}{p_o}^2\right)\left(\frac{T_o}{T}\right)^{1.5} dz \right] . \qquad (20)$$

In previous treatments of the continuum we have used exponential functions similar to those in Eqs. (18) and (20) but with the argument raised to some power less than unity.

Table 4

SELECTED PARAMETERS FOR UNIVERSAL TRANSMITTANCE MODEL AND FOR CONTINUUM REPRESENTATION

Interval (cm^{-1})	C	A	B^2	a_1	a_2	a_3	a_4
			Water Vapor				
445-465	0.5	2.03134	0.0	---	---	2.174	1.581
530-550	0.7	0.79276	0.0	---	---	1.362	0.672
700-720	0.2	0.22150	0.06542	2.518	2.081	2.471	1.935
720-740	-0.4	0.09310	0.17587	1.802	0.973	2.442	2.151
725-745	-0.4	0.17643	0.14052	2.756	2.376	2.814	2.531
735-755	0.3	0.17725	0.14711	3.263	3.207	3.053	2.883
1365-1385	0.8	2.47774	0.0	---	---	1.051	0.186
1925-1945	0.6	0.90899	0.0	---	---	1.052	0.224
2065-2085	0.8	0.21990	0.03344	1.215	-0.059	1.817	1.003
2180-2200	0.4	0.06421	1.89354	2.524	2.019	3.314	3.328
2240-2260	-0.9	0.09309	6.29549	2.770	2.377	3.695	4.057
			Uniformly Mixed Gases				
700-720	0.5	0.22782	4.29734	1.841	0.995	2.433	1.875
720-740	-2.0	0.16327	6.43306	1.521	0.476	1.946	1.097
725-745	0.8	0.09507	12.05173	1.890	1.044	2.210	1.589
735-755	0.5	0.07078	19.94220	2.351	1.698	2.883	2.581
2065-2085	0.0	0.02747	120.62780	-0.058	0.043	0.328	0.229
2180-2200	0.4	0.06970	90.38351	0.617	0.025	0.937	-0.162
2240-2260	0.9	0.22877	3.60314	0.933	0.141	1.244	0.634
			Ozone				
700-720	-0.3	0.96834	30.99535	-0.089	-0.027	-0.164	-0.019
720-740	-0.5	1.06900	46.08552	0.122	-0.095	0.167	-0.114
725-745	-0.4	0.98043	58.34086	0.134	-0.062	0.260	-0.129
735-755	-0.5	0.74925	56.89678	0.114	-0.061	0.227	-0.115
2065-2085	-0.3	0.79759	14.48916	0.416	-0.157	0.803	-0.227

	Continuum				
	C_1	C_2	C_3	C_4	C_5
445-465	156.98	1.33	0.014	-3.72	---
530-550	71.81	3.60	0.007	-2.16	---
700-720	23.881	5.60	0.002	0.0	---
720-740	21.543	5.66	0.002	0.0	---
725-745	20.986	5.68	0.002	0.0	---
735-755	19.873	5.71	0.002	0.0	---
880-900	9.185	6.08	0.002	0.0	---
1190-1210	4.609	6.08	0.002	0.0	---
1365-1385	4.175	6.08	0.002	0.0	---
1925-1945	0.67	4.56	0.12	0.0	---
2065-2085	0.54	4.56	0.12	4.56	.00024
2180-2200	0.40	4.56	0.12	4.56	.02890
2240-2260	0.33	4.56	0.12	4.56	.06595
2500-2520	0.118	4.56	0.12	4.56	.02469

VI WEIGHTING FUNCTIONS

An objective of the study was to examine several spectral intervals, distinctly separated in wavenumber, with similar transmittance weighting to the tropospheric regions where clouds are common and to the lower boundary. Differences (or lack of differences) in the multispectral radiances might then provide background information that would be useful in subsequent remote sensing of clouds themselves.

The specification of widely separated spectral intervals having identical transmittance weighting factors for the viewed earth/atmosphere is difficult to achieve, at least without the introduction of deliberate filter designs for the receiver. Without a more sophisticated system approach than that possible here it is difficult to find a precise match in response for two different intervals. Unless the absorbers played the same relative role within the two intervals, it would be likely that if a match was obtained for one condition (atmospheric structure or angle of view) the match would not hold when that condition changed. Furthermore, even if general similarity in attenuation occurred as a result of distributions of absorption lines, there would still be a requirement that the background continuum in each interval be the same (at least for low-level responses), which is relatively uncommon. At this stage of study, for intervals of about 20 cm^{-1}, only approximate matches in response were required to obtain pertinent background information.

An obvious first step in the selection of possible matching intervals in different parts of the spectrum is to examine the absorption coefficient distributions (cf. Figures 2 and 7), but this is difficult since there can be three different types of absorbers present, each with varying atmospheric distributions. Selections also can be based on the parameters derived in the transmittance modeling (cf. Table 3), but again each set of parameters refers separately to each type of absorber and does not include the continuum. Both approaches were used in this study, with the

limitation that matching be done for infrared intervals as wide as 20 cm^{-1} or more. Approximate matches could be made more nearly identical by introducing an artificial spectral filter that would force the match in response (whether or not such a filter actually could be constructed). Useful information could be derived in this way, neglecting instrument design, which is a later step.

A final check on the match between two intervals is accomplished by comparing the transmittance weighting functions themselves. This checking is done whether or not any improvement can be made. To be useful, the check must be made with the total transmittance weighting function for different conditions. The total transmittance is defined by the product of the separate transmittances for each of N absorbers and the transmittance for the continuum; that is,

$$\tau = \prod_{i=1}^{N+1} \tau_{\Delta\nu}(i) \quad . \tag{21}$$

To appreciate the choice of weighting function it is helpful to describe the radiance $R(\nu_i)$ for the ith spectral interval as measured from above the atmosphere at height H

$$R(\nu_i) = B(\nu_i, T_S)\ \tau(\nu_i, S) - \int_{z=H}^{S} B(\nu_i, T_z)\ \frac{d\tau}{dz}\, dz$$

or, by dropping the spectral identification and rewriting,

$$R = B(S)\tau(S) + \int_{S}^{H} B(z)\ \frac{d\tau(z)}{dz}\, dz \tag{22}$$

where the total transmittance τ is always measured over the path from H to the level indicated by the argument. The Planck function B(z) is defined in terms of wave number ν by

$$B(z) = C_1 \nu_i^3 / (\exp[C_2 \nu_i / T(z)] - 1) \tag{23}$$

where C_1 and C_2 are constants.

For this study $d\tau(z)/dz$ has been selected as the transmittance weighting function, with units km^{-1}. The first term on the right side of Eq. (22) depicts the contribution from the surface emission (assumed here to be blackbody) that is transmitted through the entire atmosphere. The integral represents the contribution from the molecular atmospheric emission, after being transmitted from height z to level H. Actual radiance contributions depend on the Planck function and the temperature distribution; therefore, profiles of the transmittance weighting function describe, for the molecular atmosphere, the relative weighting of Planckian contributions to the observed radiance.

The transmittance weighting function is the derivative of the transmittance with respect to the height variable. Thus, inspection of the slope of the transmittance profile can be interpreted in terms of the weighting function. Figure 8 presents the transmittance and the weighting function profiles at relatively weak and strong absorption frequencies of oxygen in the microwave region. At 52.85 GHz the trnsmittance profile shows an increasing slope below about 20 km and a slowing of the rate of decrease of transmittance near the ground. This translates to the weighting function profile shown in Figure 8, which has a maximum near the ground. At 54.9 GHz the transmittance essentially goes to zero at the ground surface, and the profile shows the steepest slope of τ with respect to z at some distance above 10 km. This profile leads to a weighting function profile with a maximum just above 10 km, with tails approaching zero both at the top and bottom. Similarly, if the attenuation is increased, as a result of either slant path viewing or an increase in the absorber, the weighting function profile is raised somewhat in altitude, with some increase in contribution at higher altitudes and, for opaque regions, a decrease in contribution at the bottom. The characteristics will be evident regardless of the wavenumber or frequency. (In keeping with conventional usage, we have retained the frequency notation for the microwave regions.)

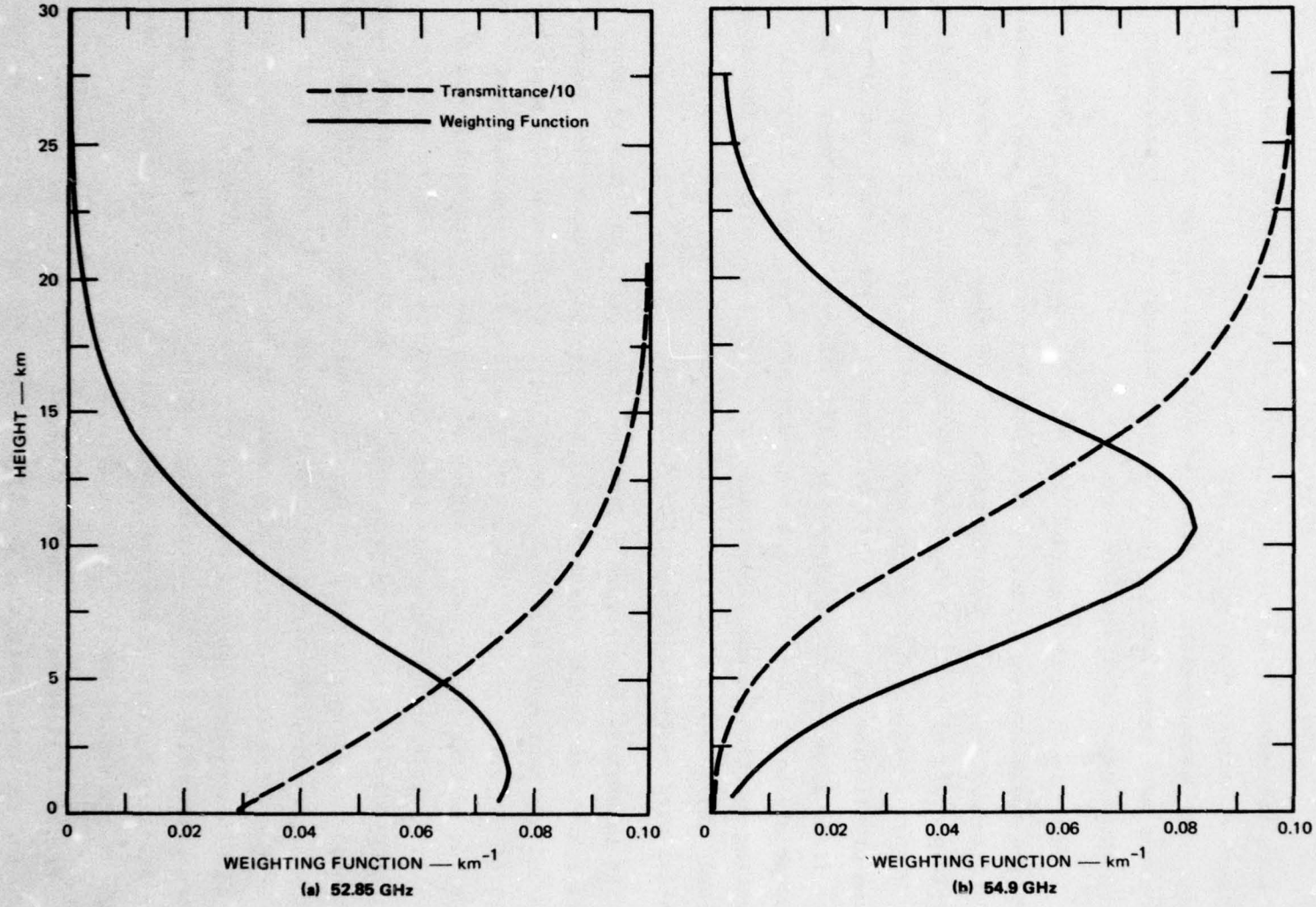

FIGURE 8 TRANSMITTANCE AND WEIGHTING FUNCTION PROFILES FOR OXYGEN AT 52.85 GHz AND 54.9 GHz

Note the smooth broad nature of the O_2 weighting function profiles in Figure 8, despite the fact that the computations are for a single frequency. The monochromatic treatment of water vapor in the microwave region shows more irregularity, in large part because of the irregularity of the water vapor distribution.

Looking again at the interval 725-745 cm^{-1}, we see that Figure 9a shows the transmittance weighting functions for each of the four component transmittances as well as for the total for the Midlatitude Summer atmospheric profile of AFGL.[16] Figure 9b shows the same thing for the Midlatitude Winter profile. Perhaps the most impressive feature is the similarity of the profile for each total with that for CO_2, even though some of the other (individual) profiles appear to be significant. It is easy to be somewhat misled by the individual component profiles, since the total weighting function is not a combination of individual weighting functions. Instead, the total transmittance must be formed, Eq. (21), before the derivative with respect to height is determined.

It is obvious from Figure 9 that the ozone plays only a very minor role, restricted to the stratosphere. Both the water vapor line absorption and the continuum have much less weight in winter than in summer because of the drier profile. Figure 10 shows the total transmittance weighting profile for 0° zenith angles in both summer and winter and for 40° zenith angle in summer. This plot illustrates variability in the weighting function, resulting from changes in profile and in viewing angle. Of course the variability depends on the amount of absorber present as well as the degree of attenuation. Figure 11a shows the variabilities for 53.5 GHz oxygen attenuation for the same conditions shown in Figure 10. Figure 11b illustrates corresponding variability for the 170-GHz water vapor transmittance weighting profile. Variations in the curve of Figure 11b are more striking because of the real seasonal change in water vapor and because of the strong low-level attenuation.

Figure 12 illustrates, for both summer and winter, the good match found for the total weighting functions of the intervals 445-465 cm^{-1} and

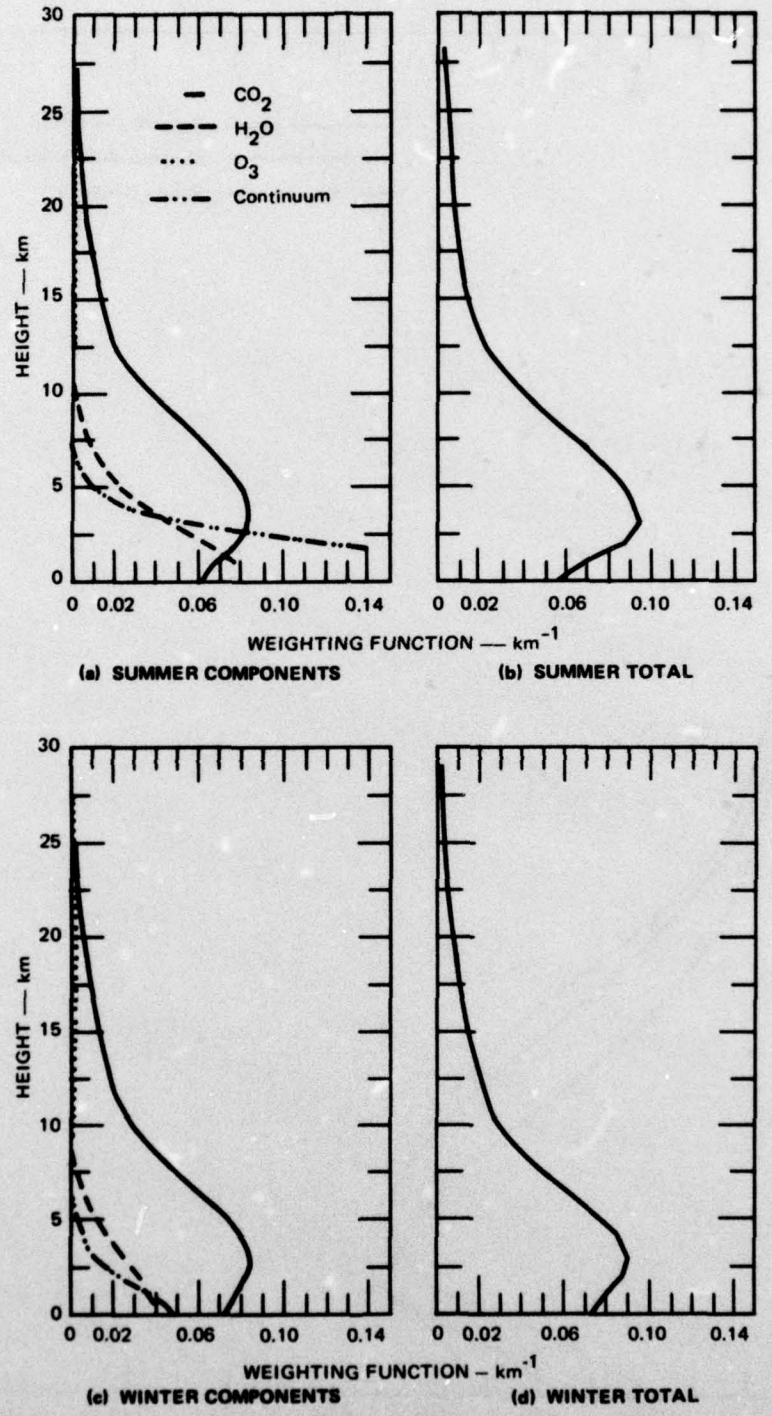

FIGURE 9 TRANSMITTANCE WEIGHTING FUNCTIONS FOR EACH CONSTITUENT AND TOTAL COMBINED TRANSMITTANCE WEIGHTING FUNCTION FOR 725-745 cm^{-1}, SUMMER AND WINTER, MIDLATITUDE

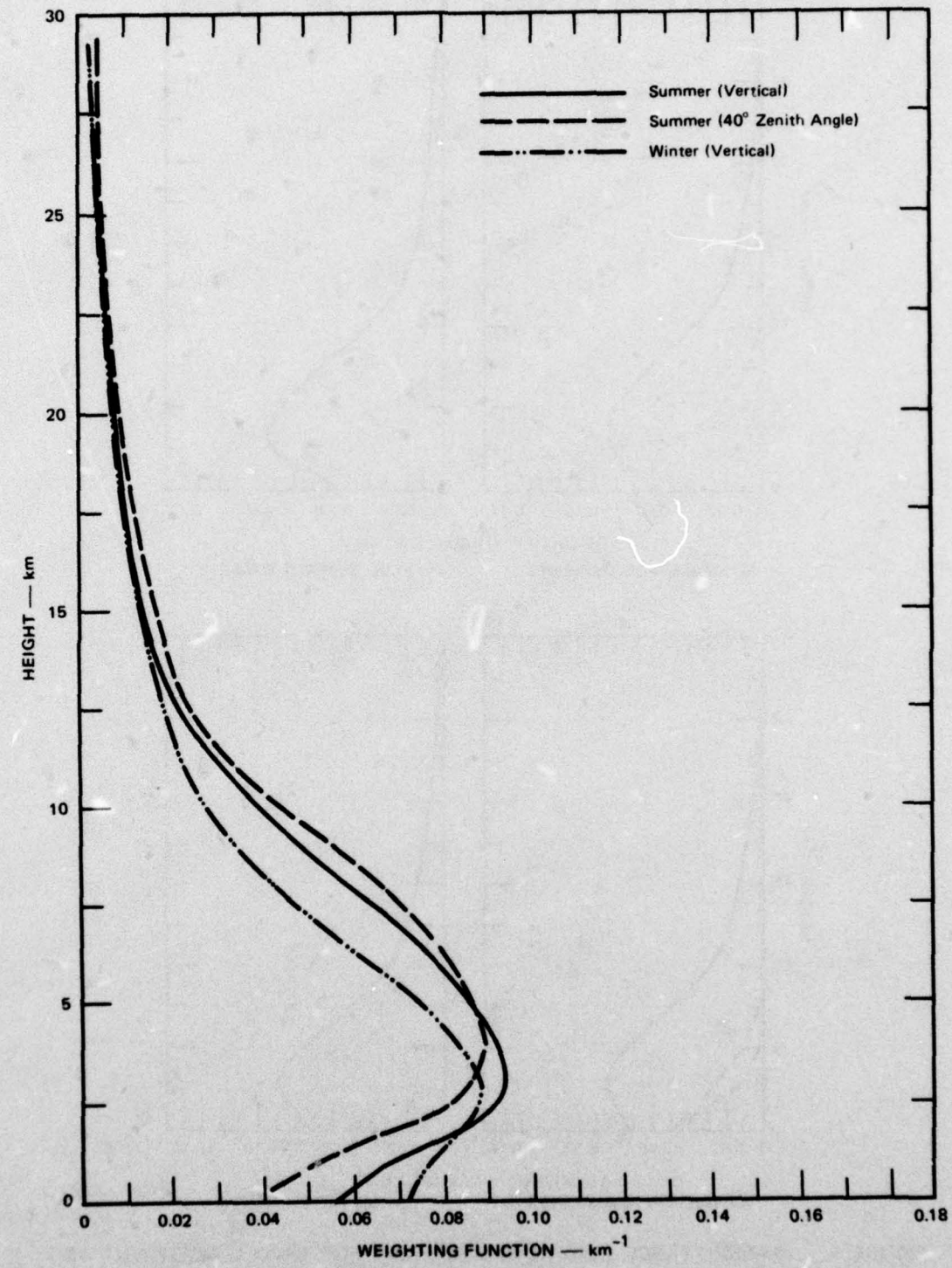

FIGURE 10 TOTAL TRANSMITTANCE WEIGHTING FUNCTIONS, 725-745 cm^{-1}

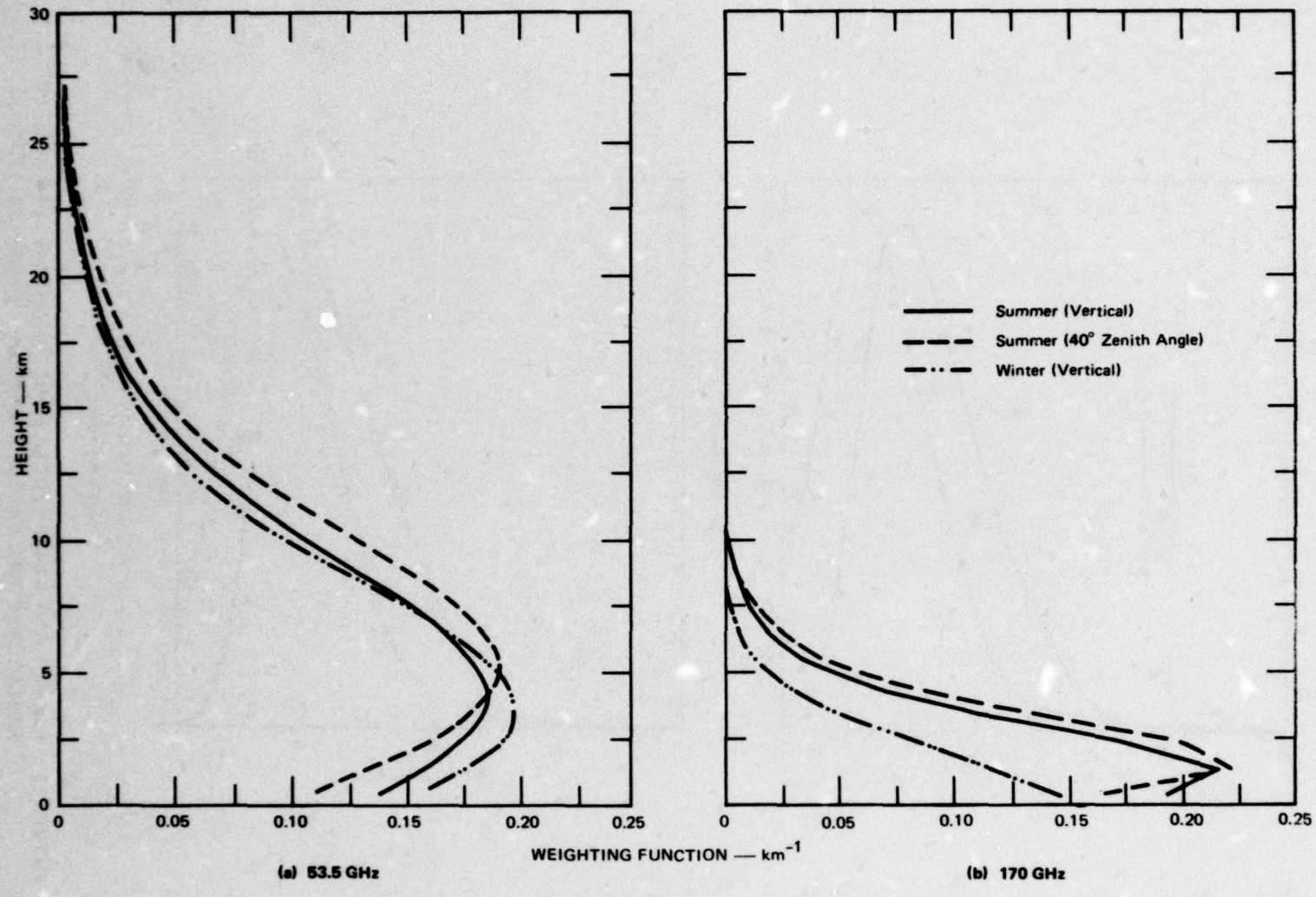

FIGURE 11 TRANSMITTANCE WEIGHTING FUNCTIONS FOR 53.5 GHz (OXYGEN) AND 170 GHz (WATER VAPOR)

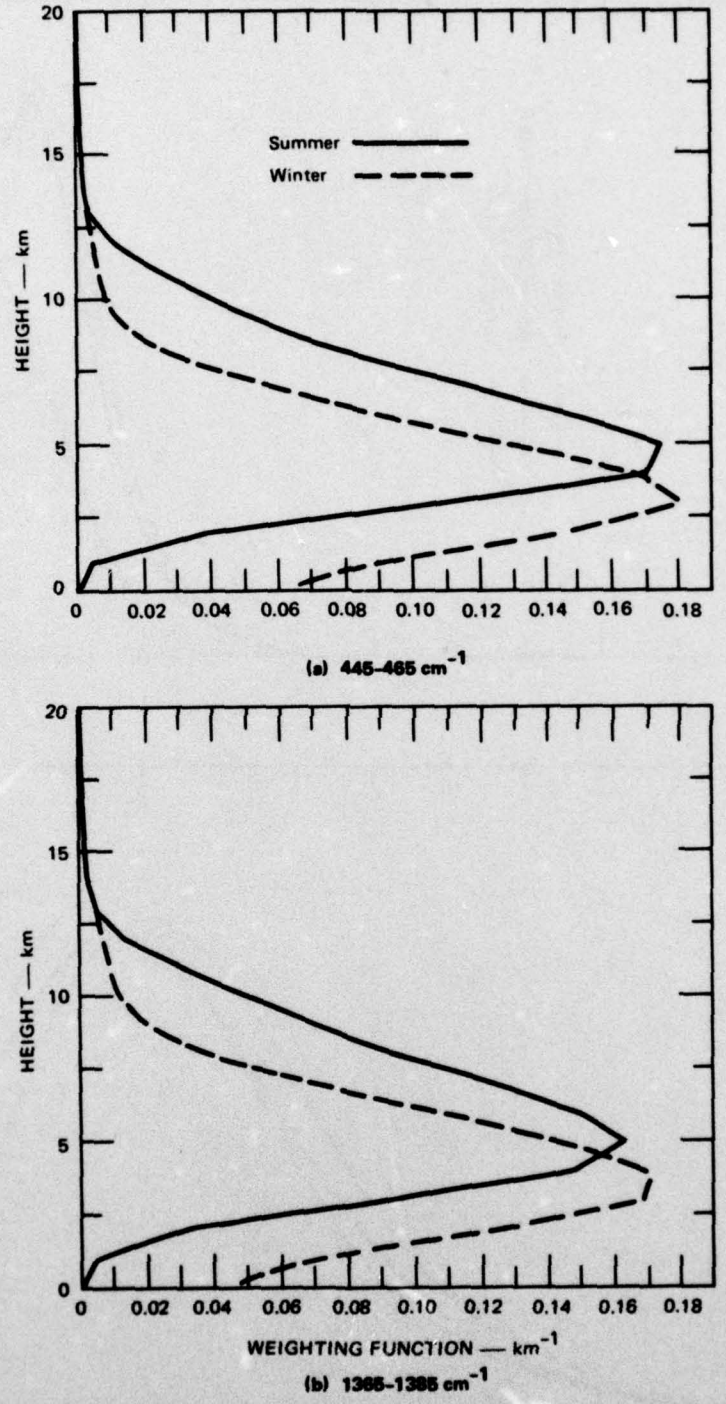

FIGURE 12 SUMMER AND WINTER PROFILES OF WEIGHTING FUNCTIONS FOR SIMILAR SPECTRAL REGIONS, 465-485 cm^{-1} AND 1365-1385 cm^{-1} VERTICAL PATHS

1365-1385 cm^{-1}, despite the much weaker continuum over the latter interval. These intervals respond to midtropospheric water vapor with essentially no surface contribution in summer.

For less strongly absorbing water vapor, Figure 13 shows an approximate match between two other 20 cm^{-1} intervals: 530-550 cm^{-1} and 1925-1945 cm^{-1}. The response from 530-550 cm^{-1} is stronger than that for 1925-1945 cm^{-1}, but the profile is very similar. In this case, it should be relatively easy to obtain an excellent match with differential filtering between radiometric channels.

The effect of changing the bandwidth from 20 cm^{-1} to 10 cm^{-1} is shown in Figures 14a and 14b for both spectral regions of Figure 13. It is seen that in both regions as the 10 cm^{-1} interval is shifted toward higher wavenumber the absorption increases. The 10 cm^{-1} profiles for 1925-1945 show blunted and relatively subdued maxima. In both cases the last interval differs in shape from the first two 10 cm^{-1} intervals. (Therefore, significant changes in the parameterization can result from changes in bandwidth.)

Better spectral matches have been obtained for other intervals. Figure 15 shows the good match between 530-550 cm^{-1} and the 178 GHz microwave frequency (water vapor) for the Midlatitude Summer profile. Figure 16 shows the apparent match between 720-740 cm^{-1} and 2180-2200 cm^{-1} at separate spectral regions commonly applied to remote sensing. As can be seen later, the larger return from the upper atmosphere in the 720-740 cm^{-1} interval prevents an actual match. In fact, despite differences in the water vapor contribution, the 2180-2200 cm^{-1} interval matches better with the 735-755 cm^{-1} interval, but that latter interval still yields lower equivalent temperatures. Figure 17 shows, for both summer and winter, the good match between weighting function profiles for 700-720 cm^{-1}, 2240-2260 cm^{-1}, and 54 GHz (oxygen). With only slight adjustments in wavenumber or frequency an even better match could be obtained (the oxygen absorption is too weak at 54 GHz to provide more response to higher altitudes).

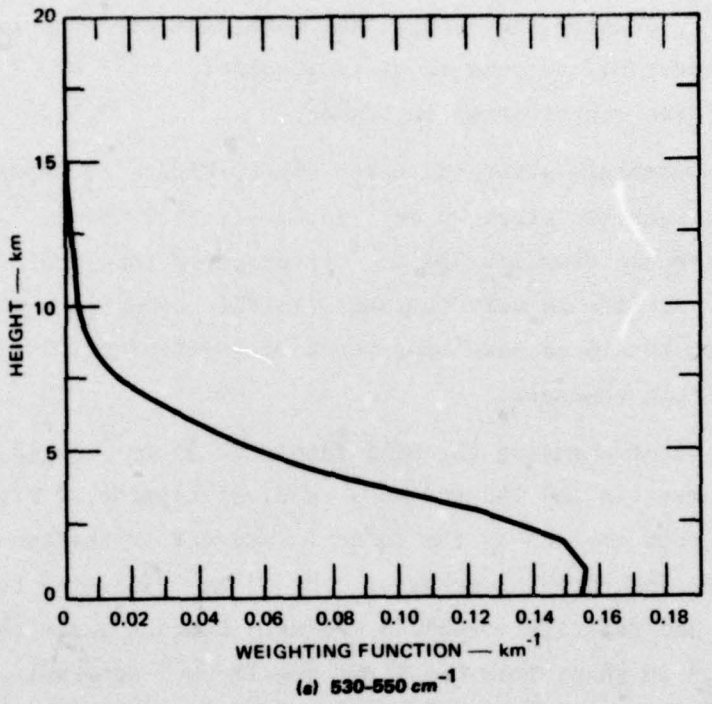

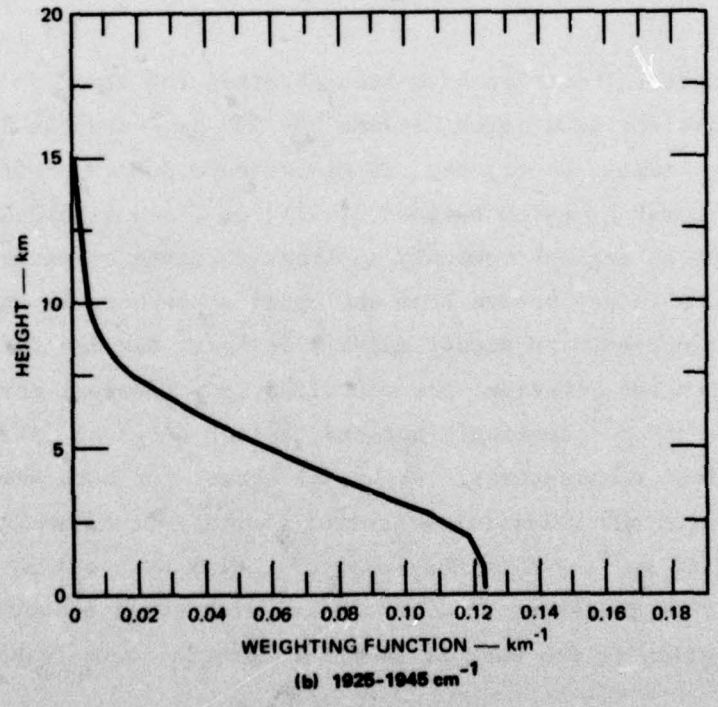

FIGURE 13 TRANSMITTANCE WEIGHTING FUNCTION COMPARISON, 530-550 cm^{-1} AND 1925-1945 cm^{-1}, WINTER PROFILES

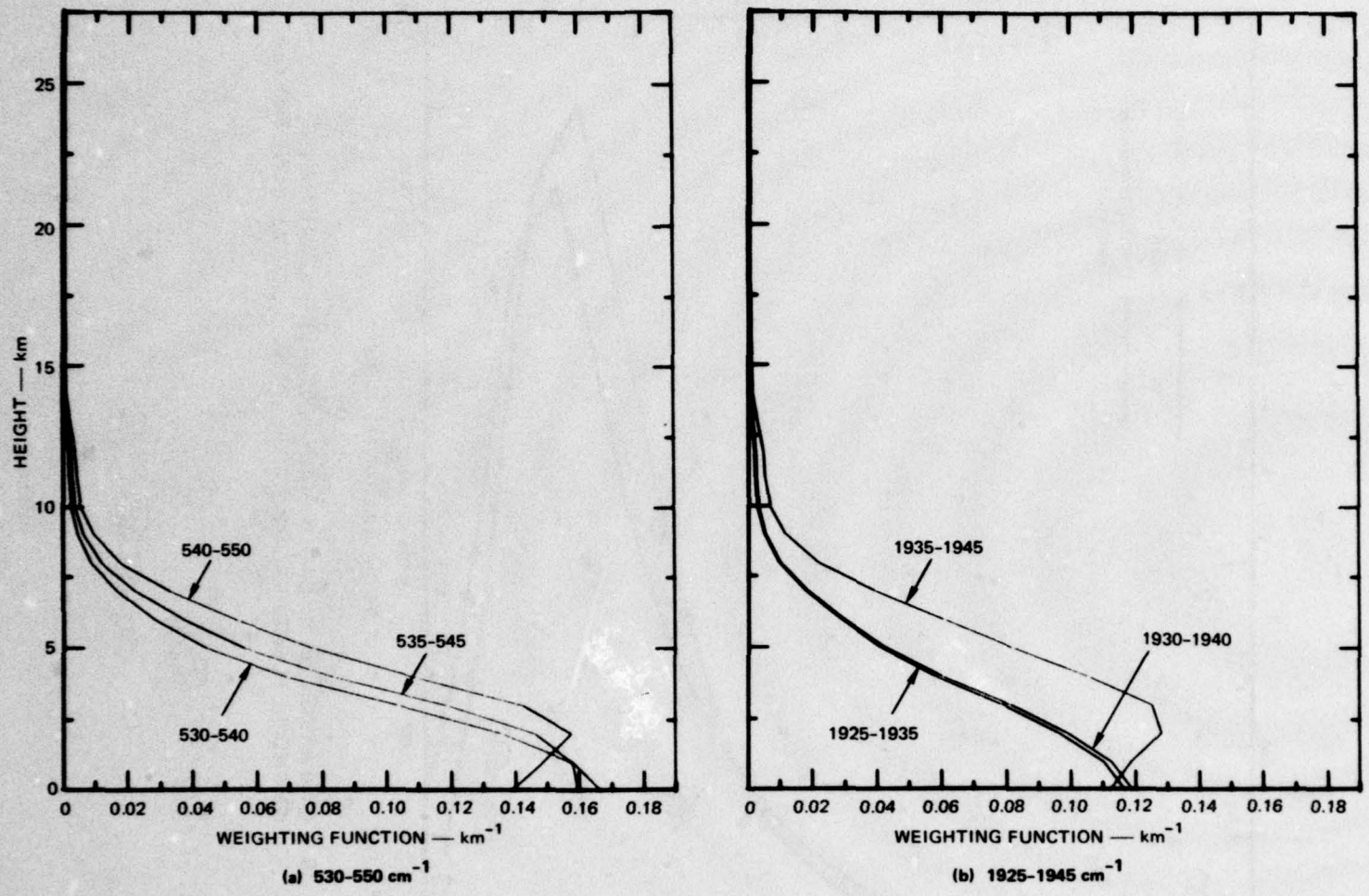

FIGURE 14 COMPARISON OF WEIGHTING FUNCTIONS FOR TWO SPECTRAL REGIONS SUBDIVIDED INTO OVERLAPPING 10 cm^{-1} INTERVALS

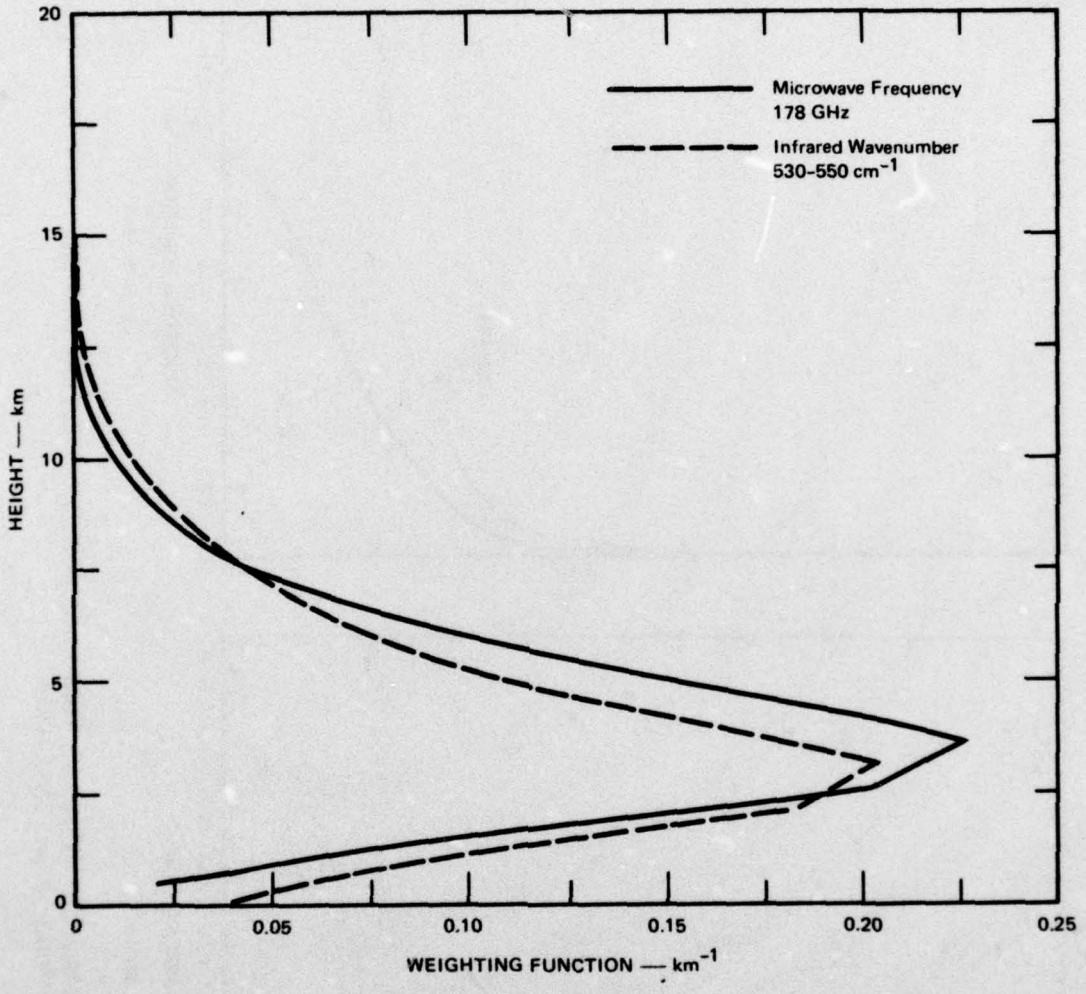

FIGURE 15 COMPARISON OF INFRARED AND MICROWAVE TRANSMITTANCE WEIGHTING FUNCTIONS FOR WATER VAPOR, VERTICAL PATH, SUMMER

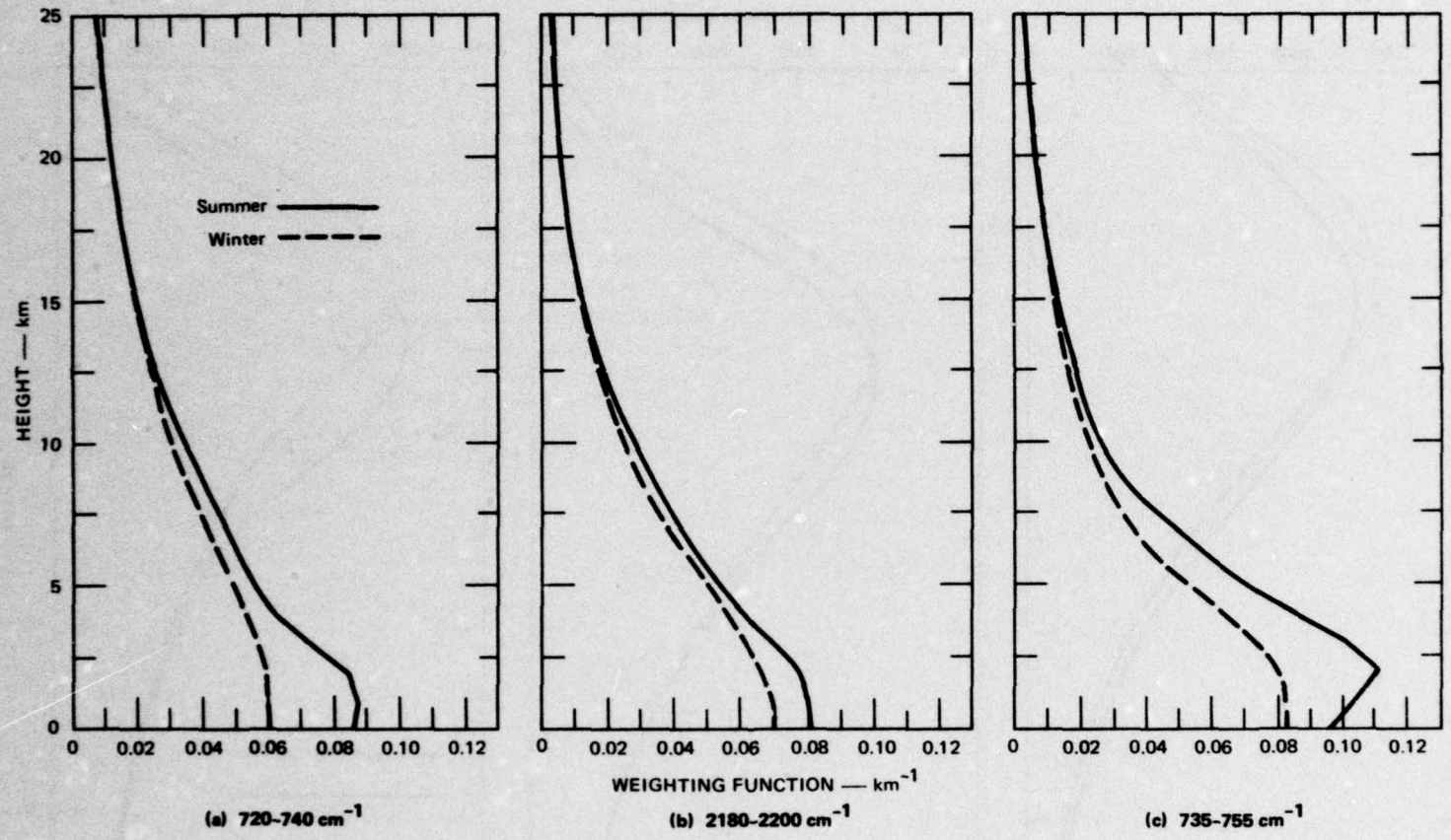

FIGURE 16 TRANSMITTANCE WEIGHTING FUNCTIONS, SUMMER AND WINTER, 720-740 cm^{-1}, 2180-2200 cm^{-1}, 735-755 cm^{-1}

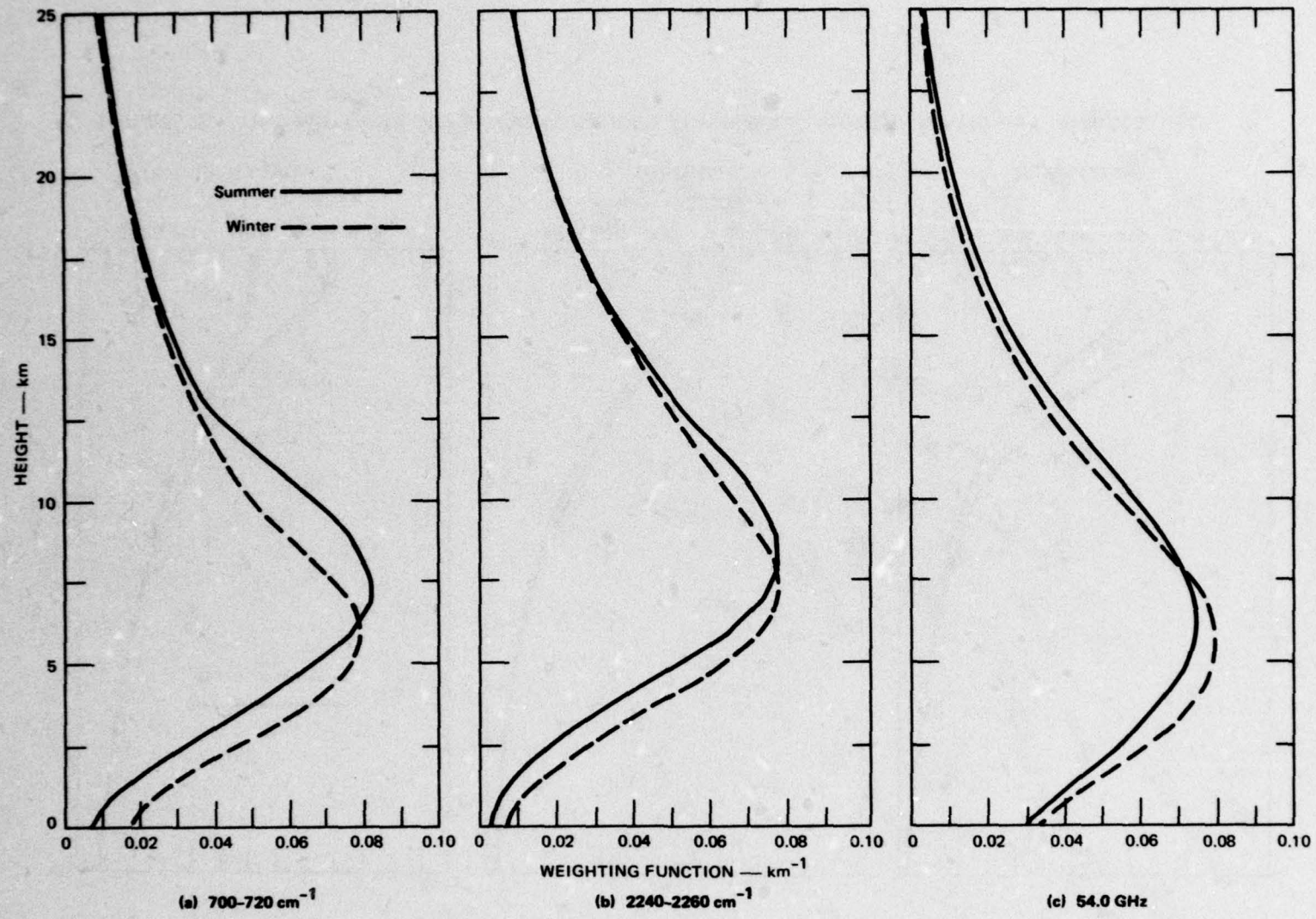

FIGURE 17 TRANSMITTANCE WEIGHTING FUNCTIONS, SUMMER AND WINTER, 700-720 cm^{-1}, 2240-2260 cm^{-1}, 54.0 GHz

Figure 18 illustrates transmittance weighting profiles for three different window regions for which only the continuum was considered. For the summer profile the 880-900 cm^{-1} absorption exceeds that for 1190-1210 cm^{-1} and 2500-2520 cm^{-1}. The latter region shows the weakest response, but with an influence over considerably more depth. This results from the nitrogen continuum peculiar to that interval. In winter the 2500-2520 cm^{-1} region shows little change while the weighting functions for the other two intervals are greatly reduced. In fact, 2500-2520 cm^{-1} shows the strongest absorption for the winter profile.

Figure 19 illustrates the transmittance weighting at three microwave frequencies. The solid curves show the computed joint transmittance for H_2O and O_2, whereas the dashed curves show the curves for H_2O only. Although the attenuation is weak in all cases, the frequency 22.235 GHz corresponds to a weak water vapor line. For H_2O only, the frequency 37 GHz shows a slightly smaller weighting function than that for 19.35 GHz. When oxygen attenuation (from the 60 GHz band) is introduced, the total weighting function is smallest at 19.35 GHz, but approximately twice as large as for H_2O alone. Additional weighting functions for H_2O and O_2 microwave frequencies are shown in Appendix C. The versatility offered by the microwave region for selection of weighting function profiles is evident.

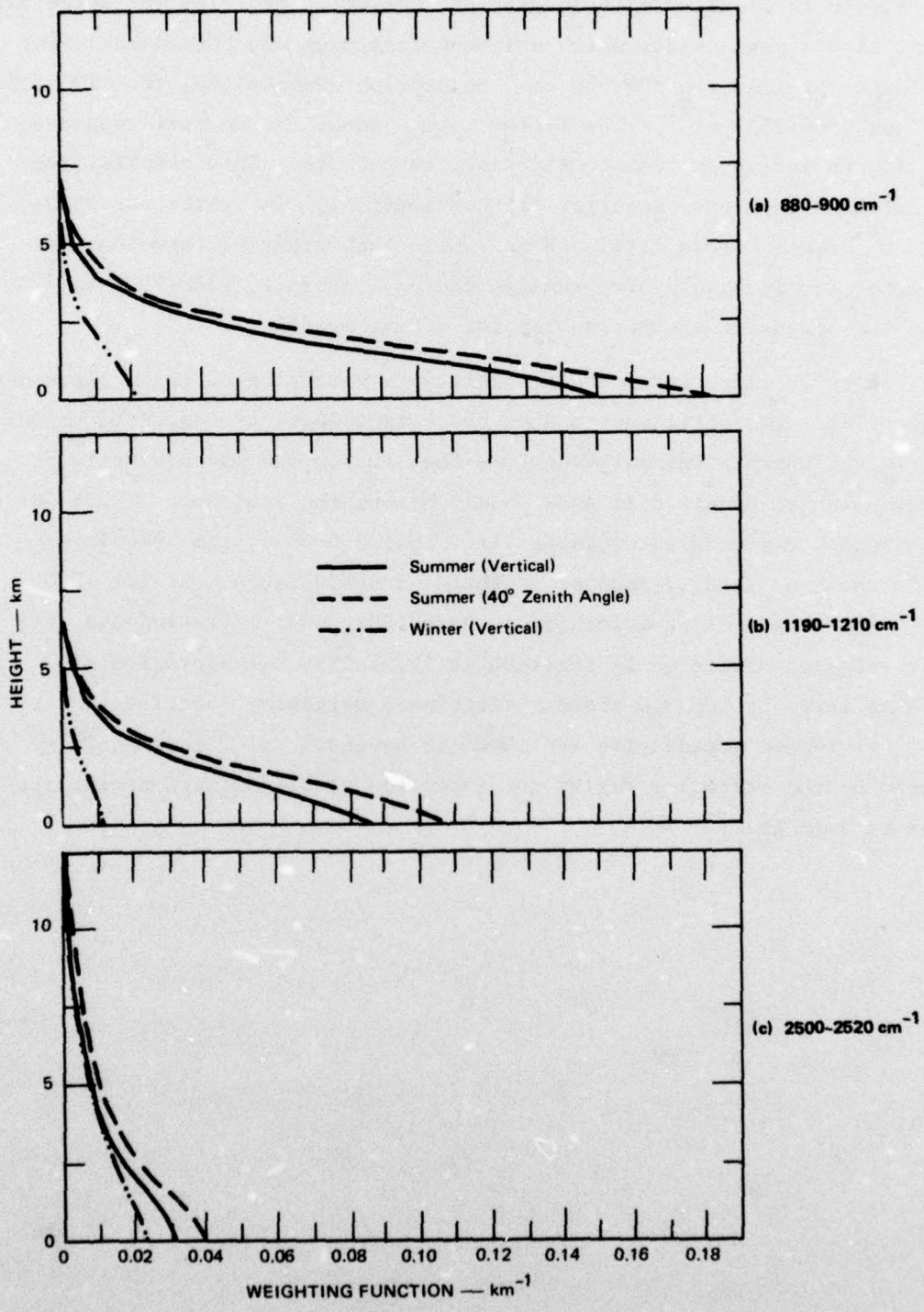

FIGURE 18 CONTINUUM TRANSMITTANCE WEIGHTING FUNCTIONS, 880-900 cm^{-1}, 1190-1210 cm^{-1}, 2500-2520 cm^{-1}

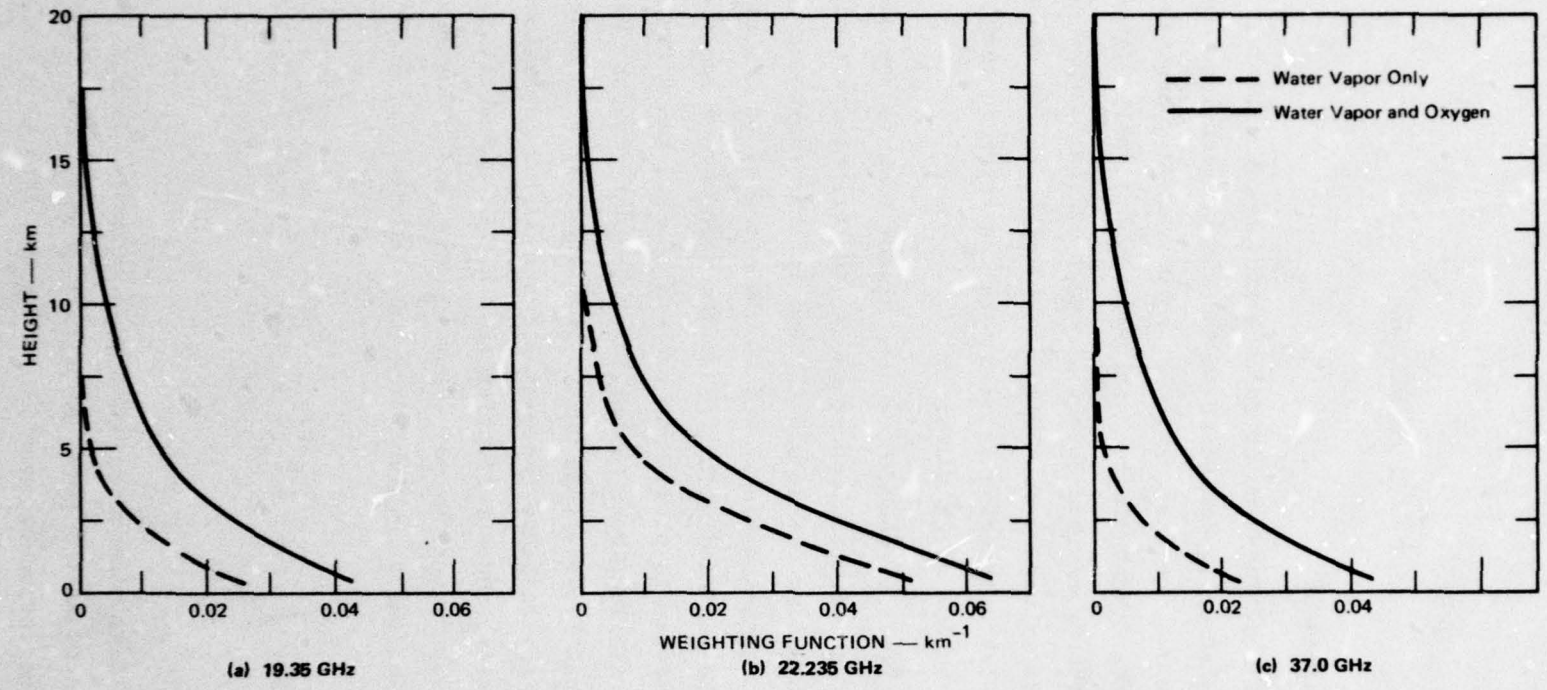

FIGURE 19 MICROWAVE TRANSMITTANCE WEIGHTING FUNCTIONS FOR FREQUENCIES OF WEAK ABSORPTION, WATER VAPOR WITH AND WITHOUT OXYGEN

VII RADIANCES

A. Upwelling Radiances

The expression of Equation 22 for the radiance received from above the atmosphere is strongly dependent on the Planck function. Because the Planck function shows a marked variation in wavenumber, especially for temperature changes, the radiances will vary considerably with wavenumber. At 300 K the blackbody maximum occurs at about 600 cm^{-1}, whereas at 200 K the blackbody maximum occurs at 400 cm^{-1}. In addition, at the higher wavenumbers the Planck function is much more sensitive to temperature differences than at low wavenumbers.

At sufficiently low frequencies, the Planck function becomes a linear function of temperature. Consequently, the brightness temperature of the microwave radiometer can be substituted for the radiance, and the Planck functions appearing singly and in the integral on the right side of Eq. (22) can be replaced with the surface temperature and the temperature from the temperature profile in the atmosphere, respectively. For microwave remote sensing, much of the lower boundary (water) has an emissivity ϵ significantly less than unity. Consequently, two changes must be introduced in the radiance expression: the surface emission must include the emissivity, and a reflection $(1 - \epsilon_s)$ of downwelling radiation at the surface must be introduced. Thus the expression for microwave measurements in Kelvins at a given frequency becomes (cf. Grody)[17]

$$T_B = \epsilon_S T_S \tau_H(S) + \int_S^H T(z) \frac{d\tau_H(z)}{dz} dz + (1 - \epsilon_S)\tau_H(S) \int_H^S T(z) \frac{d\tau_S(z)}{dz} dz \qquad (24)$$

where $\tau_H(z)$ is always measured along a path extending from H to z, $\tau_S(z)$ is always referenced at the lower boundary S, and $\tau_H(S) = \tau_S(H)$. Strictly speaking, with the introduction of an emissivity less than one, the true

weighting functions are no longer given by $d\tau_H(z)/dz$. Instead, the weighting functions are now dependent on the emissivity and on the product $\tau_H(S)\ d\tau_S(z)/dz$. This complication was not introduced in the previous illustrations.

B. Infrared Data

For the infrared computations, the lower boundary was assumed to be a blackbody. Computations were made for all 20 cm^{-1} spectral intervals involved in the matching of weighting functions. Both the Midlatitude Summer and Midlatitude Winter soundings were applied, and compuations at 0° zenith and 40° zenith angles were included for both soundings. In addition, without altering the soundings, computations were performed with the blackbody lower boundary elevated to 3, 6, and 9 km. To facilitate comparisons, each computed radiance was converted to an equivalent Planckian temperature through the inverse to Eq. (23) with the computed radiance (R) replacing the Planck radiance:

$$T_B(z) = C_2\nu_i \Big/ \log_e[(C_1\nu_i^3/R) + 1] \quad . \tag{25}$$

The height profiles of pressure and temperature defined for the two AFGL soundings are listed up to 100 km in Table 5 (densities of air, water vapor, and ozone are not repeated here). These data can be compared with the computed radiative temperatures. Tables 6a and 6b list the computed radiances and equivalent temperatures, grouped according to anticipated matches in the weighting functions. These data constitute a good set of background information (molecular atmosphere) for evaluation of relative sensing and for extended study with the introduction of cloud information. Some initial assessments can be obtained from simple manipulations of these data, as mentioned in the subsequent discussion of Subsection D.

Inspection of the radiance tables reveals that the excellent match between 445-465 cm^{-1} and 1365-1385 cm^{-1} is maintained for both viewing angles in both seasons. Water vapor dominates both spectral channels, as it does for the intervals 530-550 cm^{-1} and 1925-1945 cm^{-1}. As anti-

Table 5

HEIGHT PROFILES OF PRESSURE AND TEMPERATURE FOR MIDLATITUDE SUMMER AND MIDLATITUDE WINTER

Height (km)	Summer		Winter	
	Pressure (mb)	Temperature (K)	Pressure (mb)	Temperature (K)
0	1013	294	1018.0	272.2
1	902	290	897.3	268.7
2	802	285	789.7	265.2
3	710	279	693.8	261.7
4	628	273	608.1	255.7
5	554	267	531.3	249.7
6	487	261	462.7	243.7
7	426	255	401.6	237.7
8	372	248	347.3	231.7
9	324	242	299.2	225.7
10	281	235	256.8	219.7
11	243	229	219.9	219.2
12	209	222	188.2	218.7
13	179	216	161.0	218.2
14	153	216	137.8	217.7
15	130.0	216	117.8	217.2
16	111.0	216	100.7	216.7
17	95.0	216	86.1	216.2
18	81.2	216	73.5	215.7
19	69.5	217	62.8	215.2
20	59.5	218	53.7	215.2
21	51.0	219	45.8	215.2
22	43.7	220	39.1	215.2
23	37.6	222	33.4	215.2
24	32.2	223	28.6	215.2
25	27.7	224	24.3	215.2
30	13.2	234	11.1	217.4
35	6.52	245	5.18	227.8
40	3.33	258	2.53	243.2
45	1.76	270	1.29	258.5
50	.9510	276	.6820	265.7
70	.0671	218	.0467	230.7
100	.0003	210	.0003	210.2

Table 6

COMPUTED INFRARED RADIANCES AND EQUIVALENT TEMPERATURES
FOR TWO ANGLES OVER FOUR LOWER BOUNDARY HEIGHTS
(a) Midlatitude Summer

Spectral Interval (cm^{-1})	Surface Height (km)	0-Degree Zenith Angle Radiance $mW/(m^2sr/cm)$	0-Degree Zenith Angle Temperature (K)	40-Degree Zenith Angle Radiance $mW/(m^2sr/cm)$	40-Degree Zenith Angle Temperature (K)
700-720	0	67.450	245.45	64.055	242.49
	3	66.484	244.62	63.363	241.87
	6	63.219	241.74	60.956	239.71
	9	55.309	234.43	54.368	233.52
2240-2260	0	0.286	247.70	0.232	243.82
	3	0.273	246.80	0.226	243.29
	6	0.223	243.10	0.195	240.67
	9	0.138	233.59	0.130	233.57
720-740	0	85.527	261.90	81.763	259.04
	3	80.529	258.09	77.789	255.95
	6	69.219	248.98	67.664	247.67
	9	55.645	236.88	55.058	236.33
725-745	0	84.302	261.46	79.883	258.08
	3	80.921	258.88	77.364	256.11
	6	70.971	250.95	69.131	249.42
	9	56.478	238.21	55.858	237.63
735-755	0	90.840	267.23	86.627	264.16
	3	85.436	263.28	82.385	260.98
	6	71.895	252.73	70.339	251.45
	9	55.662	238.52	55.087	237.98
2180-2200	0	1.545	278.81	1.395	276.31
	3	1.070	270.03	0.999	268.46
	6	0.571	256.22	0.548	255.39
	9	0.247	239.92	0.243	239.57
880-900	0	106.179	292.16	105.377	291.67
	3	85.894	278.83	86.820	278.78
	6	62.577	260.99	62.562	260.98
	9	42.480	242.00	42.480	242.00
1190-1210	0	57.018	293.06	56.709	292.79
	3	42.260	278.92	42.236	278.89
	6	27.605	260.99	27.604	260.99
	9	16.416	242.00	16.416	242.00
2500-2520	0	0.829	292.81	0.816	292.45
	3	0.439	278.48	0.436	278.32
	6	0.182	260.78	0.182	260.72
	9	0.062	241.92	0.062	241.89

Table 6(a) (continued)

Spectral Interval (cm^{-1})	Surface Height (km)	0-Degree Zenith Angle Radiance $mW/(m^2sr/cm)$	0-Degree Zenith Angle Temperature (K)	40-Degree Zenith Angle Radiance $mW/(m^2sr/cm)$	40-Degree Zenith Angle Temperature (K)
445-465	0	100.248	261.79	98.325	259.94
	3	97.356	259.00	95.569	257.27
	6	94.415	256.14	93.539	255.28
	9	79.780	241.38	79.687	241.28
1365-1385	0	16.162	261.75	15.242	259.74
	3	15.520	260.35	14.703	258.51
	6	13.375	255.36	13.023	254.48
	9	8.416	240.95	8.372	240.80
530-550	0	115.700	273.05	113.323	271.19
	3	113.313	271.18	111.058	269.40
	6	98.531	259.21	98.199	258.93
	9	78.499	241.70	78.454	241.66
1925-1945	0	3.858	277.98	3.620	276.23
	3	3.185	272.76	3.072	271.80
	6	1.868	259.21	1.847	258.95
	9	0.855	241.65	0.853	241.59
530-540	0	119.770	276.23	117.449	274.42
	3	117.220	274.24	115.392	272.80
	6	99.472	259.89	99.274	259.72
	9	78.865	241.82	78.838	241.79
535-545	0	116.862	273.96	114.467	272.09
	3	114.466	272.09	112.297	270.38
	6	98.715	259.36	98.416	259.11
	9	78.510	241.71	78.466	241.67
540-550	0	111.935	270.21	109.424	268.24
	3	109.556	268.34	106.953	226.28
	6	97.222	258.40	96.727	257.99
	9	77.785	241.55	77.715	241.48
1925-1935	0	4.524	281.97	4.279	280.39
	3	3.518	274.95	3.433	274.28
	6	1.955	259.83	1.941	259.66
	9	0.880	241.77	0.878	241.74
1930-1940	0	4.387	281.60	4.144	279.98
	3	3.435	274.80	3.348	274.11
	6	1.913	259.80	1.899	259.62
	9	0.860	241.76	0.859	241.73
1935-1945	0	3.258	273.87	3.039	272.01
	3	2.818	270.02	2.687	268.79
	6	1.763	258.21	1.735	157.92
	9	0.830	241.46	0.827	241.39

Table 6 (continued)

(b) Midlatitude Winter

Spectral Interval (cm^{-1})	Surface Height (km)	0-Degree Zenith Angle Radiance $mW/(m^2 sr/cm)$	0-Degree Zenith Angle Temperature (K)	40-Degree Zenith Angle Radiance $mW/(m^2 sr/cm)$	40-Degree Zenith Angle Temperature (K)
700-720	0	57.579	236.60	54.890	234.03
	3	56.482	235.55	54.049	233.21
	6	52.138	231.33	50.712	229.91
	9	44.040	222.91	43.714	222.55
2240-2260	0	0.156	236.70	0.129	233.45
	3	0.148	235.79	0.124	232.85
	6	0.112	231.07	0.101	229.37
	9	0.066	222.61	0.064	222.21
720-740	0	69.597	249.30	66.988	247.09
	3	65.005	245.38	63.043	243.66
	6	54.242	235.54	53.282	234.62
	9	42.704	223.67	42.490	223.43
725-745	0	69.742	249.93	66.529	247.21
	3	66.262	246.98	63.788	244.84
	6	55.533	237.32	54.478	236.31
	9	42.739	224.27	42.533	224.05
735-755	0	73.879	254.34	70.968	251.97
	3	68.481	249.91	66.390	248.14
	6	55.259	238.15	54.345	237.27
	9	41.752	224.31	41.550	224.08
2180-2200	0	0.722	261.23	0.663	259.38
	3	0.527	254.58	0.496	253.33
	6	0.252	240.26	0.244	239.67
	9	0.102	224.79	0.101	224.64
880-900	0	76.378	271.94	76.275	271.86
	3	63.382	261.66	63.369	261.65
	6	44.085	243.70	44.085	243.70
	9	28.942	225.70	28.942	225.70
1190-1210	0	36.156	272.07	36.124	272.04
	3	28.091	261.68	28.087	261.68
	6	17.254	243.70	17.254	243.70
	9	9.803	225.70	9.803	225.70
2500-2520	0	0.313	271.36	0.309	271.10
	3	0.187	261.27	0.186	261.14
	6	0.068	243.54	0.068	243.49
	9	0.021	225.66	0.021	225.65

Table 6 (b) (concluded)

Spectral Interval (cm^{-1})	Surface Height (km)	0-Degree Zenith Angle Radiance $mW/(m^2sr/cm)$	0-Degree Zenith Angle Temperature (K)	40-Degree Zenith Angle Radiance $mW/(m^2sr/cm)$	40-Degree Zenith Angle Temperature (K)
445-465	0	93.209	254.96	91.694	253.46
	3	91.186	252.96	89.696	251.48
	6	81.055	242.70	80.885	242.52
	9	65.259	225.67	65.255	225.67
1365-1385	0	12.987	254.39	12.364	252.79
	3	12.250	252.49	11.746	251.15
	6	8.704	241.94	8.625	241.68
	9	4.792	225.49	4.786	225.46
530-550	0	103.188	263.06	101.721	261.85
	3	97.906	258.69	97.260	258.15
	6	80.191	243.25	80.123	243.19
	9	61.938	225.67	61.934	225.66
1925-1945	0	2.367	265.06	2.279	264.11
	3	1.838	258.82	1.805	258.39
	6	0.917	243.11	0.913	243.03
	9	0.377	225.62	0.377	225.61
530-540	0	105.932	265.22	104.645	264.17
	3	99.461	259.88	99.067	259.55
	6	80.624	243.43	80.588	243.40
	9	62.263	225.68	62.261	225.68
535-545	0	103.871	263.61	102.430	262.43
	3	98.261	258.98	97.678	258.50
	6	80.208	243.27	80.145	243.21
	9	61.935	225.66	61.930	225.66
540-550	0	100.200	260.84	98.527	259.47
	3	95.927	257.32	94.992	256.54
	6	79.382	243.00	79.270	242.89
	9	61.253	225.64	61.245	225.64
1925-1935	0	2.627	267.22	2.552	266.48
	3	1.954	259.83	1.932	259.54
	6	0.946	243.32	0.944	243.26
	9	0.387	225.65	0.387	225.64
1930-1940	0	2.561	267.06	2.485	266.29
	3	1.911	259.77	1.888	259.47
	6	0.926	243.31	0.923	243.25
	9	0.378	225.65	0.378	225.64
1935-1945	0	2.097	262.53	2.003	261.39
	3	1.699	257.43	1.656	256.81
	6	0.884	242.81	0.879	242.68
	9	0.368	225.58	0.367	225.56

cipated from the weighting function profiles discussed in Section VI, the 540 cm^{-1} spectral region is associated with stronger attenuation and, therefore, lower temperatures than the 1935 cm^{-1} region. The discrepancy in temperature is reduced in the winter because of the reduced water vapor. In the summer the discrepancy is maintained above 3 km but in winter the discrepancy is confined below 3 km. Much of the difference between channels is due to the much stronger continuum at 540 cm^{-1}.

A review of the 10 cm^{-1} intervals shows that for both the 540 and 1935 cm^{-1} regions the absorption (and weighting functions) showed an increase with wavenumber. The computed radiances show that the first two subdivisions of the 1935 cm^{-1} interval are nearly the same, with a rapid reduction for the last subdivision. In contrast, the 540 cm^{-1} subdivisions change more uniformly, and 535-545 is fairly representative of the larger 530-550 cm^{-1} interval. (Of course, the average of the intervals 530-540 and 540-550 is closest to the 530-550 result.) In this case changing the size of the interval has little impact on the radiance, but the same is not true for the 1935 cm^{-1} interval, where shrinking the interval increases the radiance.

The infrared results discussed thus far have been based on the transmittance model relating the transmittance function ψ to $A\sqrt{WP}$. With the exception of continuum transmittance, models for other spectral intervals relate ψ to $AW/[(W/P) + B^2]^{0.5}$. From Tables 6a and 6b it is apparent that the 700-720 cm^{-1} interval is well matched with the 2240-2260 cm^{-1} interval, although equivalent temperatures are a bit lower for the summer zenith position. On the other hand, the anticipated match between 720-740 cm^{-1} and 2180-2200 cm^{-1} is not there; the 720-740 cm^{-1} interval is associated with greater attenuation in the upper atmosphere and lower equivalent temperatures. Furthermore, the 725-745 cm^{-1} interval (which yields results very similar to the 720-740 cm^{-1} interval) and the 735-755 cm^{-1} interval also remain colder than the 2180-2200 cm^{-1} interval. To find a good match requires a more careful surveillance of both spectral regions.

In each of the three window intervals centered at 890, 1200, and 2510 cm^{-1}, only the continuum was considered. The 1200 cm^{-1} interval demonstrated the greatest attenuation, but in winter the decrease in water vapor meant that the 2510 cm^{-1} interval with the nitrogen continuum retained slightly higher attenuation than the 890 cm^{-1} interval. Empirical checks are needed for these channels, since it appears that all of the window channels are too transparent; greater attenuation was anticipated.

C. Microwave Data

All of the monochromatic microwave computations were performed for the same two angles for each of the same two (summer and winter) soundings, with the lower boundary taken successively at 0, 3, 6, and 9 km. However, two additional types of computations were made for each frequency. The emissivity of the lower boundary was set at 1.0, 0.5, and 0.25. Next, two types of surface reflectance were considered: specular and diffuse. For the specular reflectance, the downwelling radiance at the lower boundary was computed only at the same zenith angle as the emergent beam (cf. Grody).[17] For the diffuse reflectance, instead of multiplying the vertical optical path by the secant of the zenith angle, a factor of 1.6 was used regardless of zenith angle. This factor approximates the transformation from downward beam to flux transmittance (the main concern here was the magnitude of the departure from the specular case). A major difference is that for a comparison of radiances along the two slant paths, the downwelling radiance for the diffuse case is the same for both 0° and 40° zenith angles. This should reduce any limb brightening, but could enhance limb darkening.

Tables 7a and 7b present results for four frequencies in the oxygen band, for summer and winter; Tables 7c and 7d cover the results at four frequencies near the 183 GHz line of water vapor, and Tables 7e and 7f cover several window frequencies as well as the weak 22.235 GHz line of water vapor. Presumably, the emissivity of 1.0 would give results most consistent with viewing over land while the $\epsilon = 0.5$ might be valid for the sea surface on the average.

Table 7

COMPUTED MICROWAVE BRIGHTNESS TEMPERATURES FOR TWO ZENITH ANGLES AND VARIED SURFACE EMISSIVITY, HEIGHT, AND REFLECTANCE

(a) Oxygen, Midlatitude Summer

Lower Boundary (km)	0-Degree Zenith Angle Surface Emissivity			40-Degree Zenith Angle Surface Emissivity		
	1.0	0.5	0.25	1.0	0.5	0.25
Specular			52.85 GHz			
0	271.90	267.59	250.43	267.31	260.08	256.46
3	265.69	225.84	205.91	262.52	235.02	221.28
6	254.54	185.91	151.59	252.84	196.18	167.85
9	239.57	150.98	106.68	238.90	158.19	117.84
Diffuse						
0	271.90	264.16	260.29	267.31	261.96	259.29
3	265.69	237.44	223.32	262.52	239.34	227.75
6	254.54	197.28	168.65	252.84	201.07	175.19
9	239.57	158.57	118.07	238.90	161.72	123.14
Specular			53.5 GHz			
0	261.01	257.29	255.43	255.40	254.09	253.44
3	257.46	240.25	231.65	253.07	243.73	239.06
6	249.57	207.99	187.20	246.88	217.25	202.44
9	237.35	171.21	138.14	236.15	180.92	153.30
Diffuse						
0	261.01	259.44	258.65	255.40	254.53	254.10
3	257.46	247.46	242.47	253.07	245.91	242.34
6	249.57	219.19	204.00	246.88	221.52	208.84
9	237.35	181.63	153.77	236.15	185.44	160.08
Specular			54.0 GHz			
0	251.11	250.36	249.98	245.31	245.13	245.04
3	249.35	243.36	240.37	244.36	241.92	240.70
6	244.30	222.56	211.69	240.88	228.02	221.59
9	234.88	189.22	166.39	233.22	199.03	181.94
Diffuse						
0	251.11	250.83	250.68	245.31	245.19	245.13
3	249.35	246.49	245.06	244.36	242.65	241.79
6	244.30	230.74	223.96	240.88	230.69	225.59
9	234.88	200.10	182.70	233.22	203.35	188.42
Specular			54.9 GHz			
0	234.01	233.99	233.99	229.56	229.56	229.56
3	233.81	233.56	233.43	229.50	229.45	229.42
6	232.64	230.04	228.74	228.96	228.08	227.64
9	228.72	215.64	209.10	226.48	219.62	216.19
Diffuse						
0	234.01	234.00	234.00	229.56	229.56	229.56
3	233.81	233.70	233.64	229.50	229.46	229.44
6	232.64	231.49	230.91	228.96	228.36	228.05
9	228.72	221.35	217.66	226.48	221.30	218.70

Table 7 (continued)

(b) Oxygen, Midlatitude Winter

Lower Boundary (km)	0-Degree Zenith Angle Surface Emissivity 1.0	0.5	0.25	40-Degree Zenith Angle Surface Emissivity 1.0	0.5	0.25
Specular			52.85 GHz			
0	255.13	242.88	236.75	251.58	245.54	242.52
3	250.86	211.99	192.56	248.29	221.18	207.62
6	239.39	172.11	138.47	238.26	181.91	153.74
9	224.85	139.09	96.21	224.61	145.63	106.13
Diffuse						
0	255.13	248.72	245.52	251.58	247.19	245.00
3	250.86	223.08	209.19	248.29	225.34	213.87
6	239.39	182.61	154.22	238.26	186.49	160.60
9	224.85	145.75	106.20	224.61	148.75	110.82
Specular			53.5 GHz			
0	247.13	243.86	242.22	242.83	241.71	241.14
3	244.62	226.74	217.80	241.18	231.19	226.20
6	236.23	193.25	171.77	234.46	202.93	187.17
9	224.04	157.85	124.75	223.61	167.18	138.97
Diffuse						
0	247.13	245.81	245.15	242.83	242.10	241.74
3	244.62	234.03	228.74	241.18	233.46	229.60
6	236.23	204.12	188.07	234.46	207.19	193.55
9	224.04	167.42	139.12	223.61	171.42	145.32
Specular			54.0 GHz			
0	239.70	239.04	238.70	235.29	235.13	235.06
3	238.43	231.83	228.53	234.60	231.79	230.38
6	232.84	209.06	197.16	230.63	215.92	208.57
9	223.17	175.64	151.88	222.56	185.86	167.50
Diffuse						
0	239.70	239.46	239.35	235.29	235.19	235.14
3	238.43	235.21	233.60	234.60	232.60	231.61
6	232.84	217.57	209.93	230.63	218.81	212.90
9	223.17	186.21	167.74	222.56	190.18	173.99
Specular			54.9 GHz			
0	226.93	226.93	226.92	223.81	223.81	223.81
3	226.79	226.49	226.34	223.77	223.71	223.67
6	225.38	222.18	220.58	223.09	221.93	221.35
9	220.99	205.76	198.14	220.16	211.73	207.52
Diffuse						
0	226.93	226.93	226.93	223.81	223.81	223.81
3	226.79	226.66	226.59	223.77	223.72	223.70
6	225.38	223.95	223.24	223.09	222.29	221.90
9	220.99	212.30	207.96	220.16	213.78	210.58

Table 7 (continued)

(c) Water Vapor, Midlatitude Summer

Lower Boundary (km)	0-Degree Zenith Angle			40-Degree Zenith Angle		
	Surface Emissivity			Surface Emissivity		
	1.0	0.5	0.25	1.0	0.5	0.25
Specular			162.5 GHz			
0	286.59	271.75	264.34	284.98	277.48	273.72
3	277.30	180.55	132.18	276.82	190.12	146.77
6	260.75	137.13	75.32	260.67	139.05	78.23
9	241.98	121.74	61.62	241.97	121.96	61.96
Diffuse						
0	286.59	278.89	275.04	284.98	279.56	276.85
3	277.30	190.41	146.96	276.82	194.65	153.57
6	260.75	139.08	78.25	260.67	140.01	79.68
9	241.98	121.97	61.96	241.97	122.07	62.13
Specular			170 GHz			
0	283.58	279.68	277.72	281.63	280.28	279.60
3	276.36	198.58	159.69	275.64	210.34	177.70
6	260.60	140.97	81.16	260.48	143.93	85.66
9	241.96	122.19	62.31	241.95	122.55	62.85
Diffuse						
0	283.58	282.12	281.39	281.63	280.79	280.38
3	276.36	210.81	178.03	275.64	215.69	185.71
6	260.60	143.99	85.69	260.48	145.41	87.88
9	241.96	122.55	62.85	241.95	122.73	63.12
Specular			178 GHz			
0	272.17	272.17	272.17	269.71	269.71	269.71
3	270.47	255.49	247.99	268.66	260.92	257.05
6	259.41	167.52	121.58	258.97	176.24	134.88
9	241.85	125.87	67.88	241.80	127.29	70.03
Diffuse						
0	272.17	272.17	272.17	269.71	269.71	269.71
3	270.47	262.48	258.48	268.66	262.99	260.16
6	259.41	176.51	135.05	258.97	180.39	141.10
9	241.85	127.31	70.04	241.80	128.00	71.10
Specular			182 GHz			
0	252.13	252.13	252.13	249.53	249.53	249.53
3	252.13	252.13	252.13	249.53	249.53	249.53
6	250.69	242.25	238.03	248.73	244.95	243.06
9	240.47	161.53	122.06	240.05	170.59	135.86
Diffuse						
0	252.13	252.13	252.13	249.53	249.53	249.53
3	252.13	252.13	252.13	249.53	249.53	249.53
6	250.69	246.69	244.69	248.73	246.11	244.80
9	240.47	170.84	136.02	240.05	174.81	142.19

Table 7 (continued)

(d) Water Vapor, Midlatitude Winter

Lower Boundary (km)	0-Degree Zenith Angle Surface Emissivity 1.0	0.5	0.25	40-Degree Zenith Angle Surface Emissivity 1.0	0.5	0.25
Specular			162.5 GHz			
0	269.76	206.23	174.46	269.12	218.54	193.25
3	261.11	147.34	90.46	260.94	151.84	97.29
6	243.65	123.56	63.51	243.63	124.07	64.28
9	225.70	112.99	56.64	225.70	113.03	56.70
Diffuse						
0	269.76	218.98	193.59	269.12	223.89	201.28
3	261.11	151.93	97.35	260.94	154.07	100.63
6	243.65	124.07	64.29	243.63	124.32	64.67
9	225.70	113.03	56.70	225.70	113.05	56.73
Specular			170 GHz			
0	268.51	227.79	207.43	267.60	239.21	225.02
3	260.76	156.14	103.82	260.50	162.65	113.73
6	243.61	124.59	65.07	243.59	125.39	66.30
9	225.69	113.08	56.77	225.69	113.15	56.87
Diffuse						
0	268.51	239.90	225.60	267.60	243.80	231.89
3	260.76	162.80	113.82	260.50	165.82	118.48
6	243.61	125.41	66.30	243.59	125.80	66.91
9	225.69	113.15	56.87	225.69	113.18	56.93
Specular			178 GHz			
0	262.14	260.16	259.17	260.40	259.82	259.53
3	258.34	202.79	175.02	257.48	214.48	192.99
6	243.36	132.51	77.09	243.25	135.51	81.64
9	225.68	113.80	57.87	225.67	114.09	58.29
Diffuse						
0	262.14	261.48	261.16	260.40	260.06	259.89
3	258.34	215.08	193.45	257.48	219.53	200.55
6	243.36	135.57	81.67	243.25	137.01	83.88
9	225.68	114.09	58.30	225.67	114.23	58.51
Specular			182 GHz			
0	247.77	247.77	247.77	245.46	245.46	245.45
3	247.53	246.24	245.59	245.36	245.00	244.82
6	240.89	182.67	153.56	240.16	193.48	170.13
9	225.43	122.94	71.70	225.36	125.78	76.00
Diffuse						
0	247.77	247.77	247.77	245.46	245.46	245.45
3	247.53	247.09	246.86	245.36	245.14	245.03
6	240.89	193.97	170.51	240.16	198.24	177.28
9	225.43	125.82	76.02	225.36	127.19	78.11

Table 7 (continued)

(e) Oxygen-Water Vapor, Midlatitude Summer

Lower Boundary (km)	0-Degree Zenith Angle Surface Emissivity 1.0	0.5	0.25	40-Degree Zenith Angle Surface Emissivity 1.0	0.5	0.25
			19.35 GHz			
Specular						
0	290.16	190.88	141.23	289.08	200.80	156.66
3	277.02	159.23	100.34	276.45	164.48	108.49
6	260.11	139.79	79.63	259.85	142.42	83.70
9	241.68	125.35	67.19	241.58	126.63	69.15
Diffuse						
0	290.16	201.47	157.13	289.08	205.64	163.91
3	277.02	164.79	108.68	276.45	167.15	112.51
6	260.11	142.56	83.78	259.85	143.78	85.74
9	241.68	126.67	69.17	241.58	127.28	70.13
			22.235 GHz			
Specular						
0	288.63	210.85	171.97	287.17	222.88	190.73
3	276.43	167.92	113.66	275.69	175.04	124.72
6	259.94	142.77	84.19	259.62	146.18	89.46
9	241.66	126.39	68.76	241.55	127.96	71.16
Diffuse						
0	288.63	223.87	191.49	287.17	228.49	199.15
3	276.43	175.47	124.99	275.69	178.61	130.06
6	259.94	146.35	89.55	259.62	147.93	92.08
9	241.66	128.01	71.18	241.55	128.76	72.36
			31.4 GHz			
Specular						
0	290.01	190.93	141.40	288.88	200.84	156.83
3	276.90	159.86	101.34	276.29	165.24	109.72
6	260.04	140.38	80.55	259.76	143.17	84.87
9	241.65	125.70	67.72	241.55	127.07	69.83
Diffuse						
0	290.01	201.55	157.32	288.88	205.69	164.09
3	276.90	165.58	109.92	276.29	167.99	113.84
6	260.04	143.32	84.95	259.76	144.61	87.03
9	241.65	127.12	69.85	241.55	127.77	70.88
			37.0 GHz			
Specular						
0	289.67	193.61	145.58	288.46	203.88	161.59
3	276.71	161.49	103.88	276.05	167.24	112.84
6	259.96	141.25	81.90	259.65	144.27	86.58
9	241.62	126.12	68.38	241.50	127.61	70.67
Diffuse						
0	289.67	204.65	162.14	288.46	208.88	169.09
3	276.71	167.61	113.06	276.05	170.17	117.23
6	259.96	144.43	86.67	259.65	145.82	88.91
9	241.62	127.67	70.70	241.50	128.38	71.81

Table 7 (concluded)

(f) Oxygen-Water Vapor, Midlatitude Winter

Lower Boundary (km)	0-Degree Zenith Angle Surface Emissivity 1.0	0.5	0.25	40-Degree Zenith Angle Surface Emissivity 1.0	0.5	0.25
Specular			19.35 GHz			
0	269.28	172.71	124.42	268.45	181.31	137.74
3	260.02	148.94	93.40	259.54	153.77	100.89
6	243.08	130.46	74.15	242.90	132.90	77.90
9	225.58	116.73	62.30	225.55	117.86	64.02
Diffuse						
0	269.28	181.81	138.07	268.45	185.51	144.04
3	260.02	154.04	101.04	259.54	156.23	104.57
6	243.08	133.00	77.95	242.90	134.15	79.78
9	225.58	117.88	64.03	225.55	118.43	64.88
Specular			22.235 GHz			
0	268.79	179.68	135.13	267.84	189.34	150.09
3	259.79	152.19	98.39	259.24	157.76	107.02
6	243.02	131.64	75.95	242.81	134.40	80.19
9	225.59	117.46	63.40	225.56	118.81	65.43
Diffuse						
0	268.79	189.94	150.51	267.84	193.99	157.06
3	259.79	158.07	107.20	259.24	160.57	111.24
6	243.02	134.50	80.25	242.81	135.80	82.30
9	225.59	118.82	65.44	225.56	119.48	66.44
Specular			31.4 GHz			
0	269.08	174.53	127.26	268.20	183.42	141.03
3	259.90	150.07	95.16	259.37	155.17	103.06
6	243.03	131.12	75.17	242.83	133.75	79.20
9	225.58	117.05	62.78	225.54	118.27	64.64
Diffuse						
0	269.08	183.96	141.40	268.20	187.75	147.53
3	259.90	155.45	103.23	259.37	157.75	106.93
6	243.03	133.85	79.26	242.83	135.08	81.20
9	225.58	118.29	64.65	225.54	118.89	65.57
Specular			37.0 GHz			
0	268.80	177.34	131.60	267.85	186.64	146.04
3	259.73	151.68	97.65	259.17	157.13	106.11
6	242.97	131.95	76.43	242.76	134.79	80.80
9	225.56	117.43	63.36	225.52	118.76	65.39
Diffuse						
0	268.80	187.23	146.45	267.85	191.16	152.81
3	259.73	157.44	106.30	259.17	159.89	110.25
6	242.97	134.90	80.86	242.76	136.23	82.97
9	225.56	118.78	65.40	225.52	119.44	66.39

The results for the oxygen computations show, as expected, significant attenuation that increases as the center of the band is approached. The lower response in winter reflects the lower temperatures for that season. As required, results for specular and diffuse surface reflectors are identical for all lower boundary altitudes when the surface emissivity is 1.0 (no reflectance). All results show a limb darkening that decreases as the boundary altitude increases. With the surface emissivity set at 0.5, and looking first at summer results with the lower boundary at 0 km, all computations show a limb darkening except for the 52.85 GHz frequency with the specular surface. Here the increased downwelling radiance at 40° zenith angle (relative to the 0° zenith angle) and the resulting increased upward reflected radiance with less attenuation than at the other frequencies, produce a limb brightening. It also is apparent that the brightness temperature for the radiance above the diffuse surface exceeds that above the specular surface, especially for the zenith direction. Since this enhancement results from the larger downwelling radiance, the effect varies with the altitude of the surface and with the degree of attenuation for the given frequency. The height at which the maximum difference occurs increases as the attenuation increases. A similar sort of pattern prevails for the surface with a 0.25 emissivity. It is noteworthy that with the surface elevated and at reduced emissivity the emergent radiances show a limb brightening for the two lowest frequencies. This brightening is most pronounced over the specular surface because of the change in the downwelling radiance, and can reach substantial magnitudes. Presumably, it would be possible to test empirically which type of reflecting surface corresponds most closely with observation. Because most elevated surfaces would not be likely to possess an emissivity much different from unity, comparisons probably should be based only on surfaces at 0 km elevation. For that situation, and with relatively weak atmospheric attenuation, significantly reduced limb brightening (or enhanced darkening) occurs over the diffuse surface.

The above discussion applies also to the winter situation and is generally consistent with the results obtained as the 183 GHz line of water vapor is approached (with increasing attenuation). However, the

brightness temperatures at the water vapor frequencies generally are higher for $\epsilon = 1$ and for all ϵ at $z = 0$ in summer, with a more rapid decrease at higher boundary elevations when $\epsilon < 1$. In winter, with less water vapor, temperatures decrease much more rapidly than for O_2 as ϵ is reduced, as well as when the height of the boundary is increased.

For the weak 22.235 water vapor line and three nearby window regions, the brightness temperatures are summarized for the same conditions as before, and results are compatible with what might be expected for weak attenuation. When the surface emissivity is reduced to 0.5 or 0.25, limb brightening is evident everywhere (even with the 0 km boundary), and is smallest over the diffuse surface. Differences between surface types are not as pronounced as with some of the previous cases. Although window brightness temperatures are high for the blackbody surface at 0 km, the temperature decreases more rapidly with elevation of the boundary and with reduction of the emissivity than at frequencies with greater attenuation. (High boundaries with low emissivities are not realistic.)

The 19.35 GHz frequency shows the strongest return over a blackbody surface (for the O_2-H_2O combination) but results are not much different between channels, including the 22.235 frequency. For the surface at 0-km altitude the brightness temperature over the diffuse surface is distinctly larger.

D. Clouds

Without computations from an appropriate physical cloud model* it is not possible to draw inferences concerning cloud physical and radiative properties (cf. Curran[18]) from the radiances already compiled. On the other hand, from the infrared radiances it is possible to draw some general conclusions. In the infrared it is not unreasonable to treat the lower boundary as a blackbody (emissivity equals unity). Also, for a specified altitude "effective" amounts of blackbody clouds can be introduced. The effective amount is actually a product of the amount and the

*Beyond the scope of this study

emissivity, although apparent emissivity often includes subresolution cloud holes. Thus, a 0.5 cover of cloud with a 0.5 emissivity could be associated with the same radiance as 0.25 cover of blackbody cloud at the same altitude.

All of the radiances listed in Table 6 can be manipulated with the above assumption. Tabulations were made with a blackbody lower boundary at 0, 3, 6, and 9 km. The elevated surfaces might be used to represent low, middle, and high clouds. Any effective amount can be assigned. For example, if 0.5 cover of cloud at 6 km is assumed, the "measured" radiance would be equal to 0.5 of the tabulated results for 6 km and 0.5 of the results for 0 km. The sum of the weighted radiances can then be converted to temperature with the aid of Eq. (25).

When this type of analysis is pursued, it becomes apparent that the infrared channels are responsive to the effects of high clouds but unresponsive to small changes near the lower boundary. Multispectral techniques[17,20] that have been applied or suggested for the derivation of cloud height or amount have not required matched spectral responses. The real merit of matched responses is in application to the detection of known spectral variations of homogeneous cloud radiative properties established through a proper model. The only other advantage is that matched sensors will respond differently to a nonhomogeneous scene because of the spectral variation of the sensitivity of the Planck function with temperature.

As an example of the use that can be made of data in the radiance tables, consider the spectral regions centered at 455, 540, and 1935 cm^{-1}. The regions at 540 and 1935 cm^{-1} have already been examined with respect to their weighting functions in winter. From the midlatitude winter data new radiances (and equivalent temperatures) were formulated from the tabulations to correspond to 0, 0.25, 0.5, 0.75, and 1.0 equivalent blackbody cloud cover at the 3, 6, and 9 km altitudes. Figure 20 is a plot of the joint radiances (listed in Table 8) for the 455 cm^{-1} and 540 cm^{-1} channels. The heavy dashed curve connects joint radiances for uniform complete blackbody coverage at each of the indicated altitudes. Also

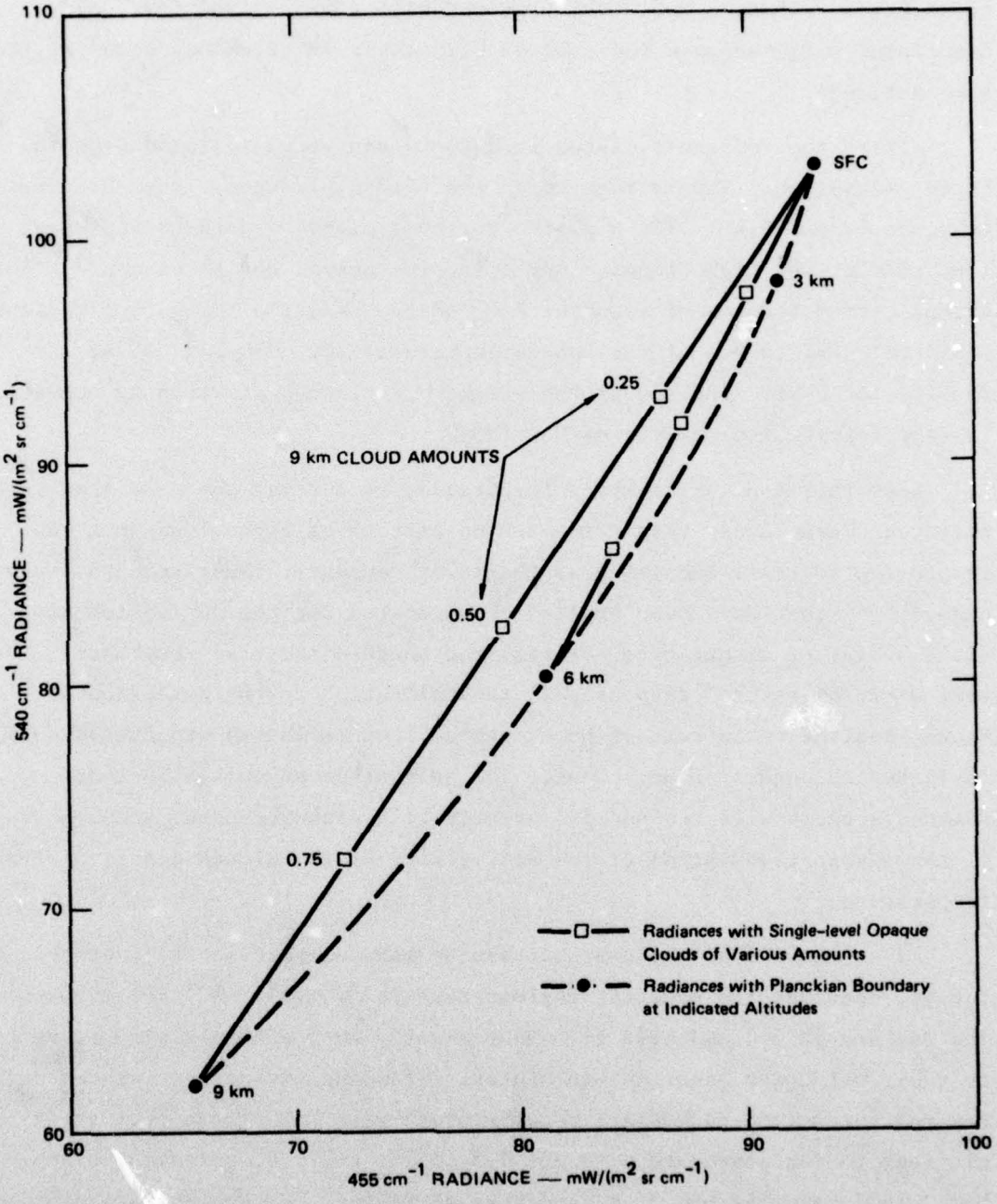

FIGURE 20 APPLICATION OF RADIANCES FROM TWO INFRARED CHANNELS TO IDEALIZED CLOUD ANALYSIS (MIDLATITUDE SUMMER ATMOSPHERE)

Table 8

SELECTED RADIANCES FOR INDICATED CLOUD AMOUNTS
AT THREE ALTITUDES

Cloud Amount	Radiances ($mW\ m^{-2}\ sr^{-1}\ (cm^{-1})^{-1}$)								
	475 cm^{-1}			540 cm^{-1}			1935 cm^{-1}		
	3 km	6 km	9 km	3 km	6 km	9 km	3 km	6 km	9 km
.00	93.209	93.209	93.209	103.188	103.188	103.188	2.367	2.367	2.367
.25	92.704	90.171	86.222	101.868	97.439	92.876	2.235	2.004	1.869
.50	92.198	87.133	79.235	100.547	91.690	82.563	2.103	1.643	1.373
.75	91.692	84.093	72.246	99.227	85.940	72.251	1.971	1.280	0.875
1.00	91.186	81.055	65.259	97.906	80.191	61.938	1.838	0.917	0.377

plotted by small boxes and joined with straight lines are the joint radiances at 6 km and 9 km for each of the cloud amounts. When the cloud height is held fixed, all of the radiances fall on a straight line connecting the joint clear column radiance and the joint radiance for complete coverage at the given altitude (both points on dashed curve). The fraction of distance along the connecting line also indicates the amount of effective cloud cover. (If the plots are made in equivalent temperatures, then the points do not divide the joining line by portions equivalent to amounts.) It is obvious that it would be difficult to get information at low altitudes, and that the ease of information extraction increases with altitude. The plots have been made on the assumption of single cloud layers without serious noise in measurements.

Whether or not the information from 1935 cm^{-1}, for example, which nearly matches 540 cm^{-1} in response, is really helpful or necessary in dealing with amount or height of equivalent cloud has not been ascertained. However, it is possible to establish some difference in temperature response to a partial cloud cover.

Since the Planck function is much more sensitive to temperature difference at higher wave numbers (higher frequencies) than at low wave numbers, the warmer (clear) portions of a partly cloudy scene will contribute

relatively more to the total radiance at 1935 cm^{-1} than at 540 cm^{-1}. In other words, the Planck function for the 1935 cm^{-1} interval should translate to a higher equivalent temperature over a nonhomogeneous scene than that for the 540 cm^{-1} interval, even with a perfect match in the responses for both intervals when viewing homogeneous backgrounds. Although the responses for the two intervals are not perfectly matched, the concept of the differing equivalent temperature can be demonstrated from the computed radiances in Table 8. If T_0 represents the equivalent temperature for clear skies with the surface at 0 km, T_c indicates the equivalent temperature for a complete opaque overcast at the indicated altitude, and T_6 or T_9 represents the equivalent temperature for a partial cloud cover at 6 km or 9 km, then the following temperature ratios are obtained for three partial cloud covers:

	540 cm^{-1}		1935 cm^{-1}	
	(6 km)	(9 km)	(6 km)	(9 km)
Cloud Amount	$\left[\frac{T_0-T_6}{T_0-T_c}\right]$	$\left[\frac{T_0-T_9}{T_0-T_c}\right]$	$\left[\frac{T_0-T_6}{T_0-T_c}\right]$	$\left[\frac{T_0-T_9}{T_0-T_c}\right]$
0.25	.23	.23	.19	.15
0.50	.48	.47	.40	.33
0.75	.74	.73	.67	.58
	T_0 = 262.9	262.9	T_0 = 265.1	265.1
	T_c = 243.3	225.7	T_c = 243.1	225.7

A study of these results reveals relatively higher equivalent temperatures at 1935 cm^{-1} (in comparison to 540 cm^{-1}) for partial cloud covers, with the greatest differences for the highest clouds. Since responses were not perfectly matched, the equivalent temperature (T_0) for 1935 cm^{-1} over a homogenous surface under clear skies was 2.2k higher than for 540 cm^{-1}. With an opaque uniform cloud cover at 9 km the equivalent temperatures (T_c) for the overcast state were the same. When partial cloud covers are introduced at 9 km, it is apparent that at 1935 cm^{-1} only 15%

of the total clear-overcast temperature decrease occurs by 25% of the possible cloud cover, and only 33% of the temperature decrease occurs as the cloud cover is increased to 50 percent. Comparable figures for 540 cm are 23% and 47% of the total temperature decrease. Since the percentage temperature decline is smaller at 1935 cm^{-1} for each quartile of cloud amount, the temperatures are remaining relatively higher. The excess of equivalent temperature at 1935 cm^{-1} over that at 540 cm^{-1} increases from 2.2K for clear skies to a maximum of 6.7K for 50 percent cloud cover.

VIII CONCLUSIONS

This study has demonstrated the feasibility of modeling simplified but reliable transmittance representations, over infrared spectral intervals on the order of 20 wavenumbers, for applications to the nonhomogeneous molecular atmosphere. Parameterizations, which include temperature-dependent scaling coefficients, are based on detailed monochromatic absorption coefficients computed from pertinent absorption-line parameters at a variety of pressures and temperatures. Data and the transmittance-radiance models are available for extension, refinement, and empirical testing as well as for introduction into a meaningful software system package for future design studies.

The transmittance representations were used in the generation of background information that documents radiance variations with changes in spectral position, atmospheric structure, viewing angle, and boundary conditions. Infrared radiances and their equivalent temperatures that were simulated in the presence of opaque surfaces at various altitudes may be examined to infer gross effects of cloud height and amount. The higher the effective opaque surface, the more responsive were the infrared sensors. The microwave brightness temperatures and their limb variations over surfaces with reduced emissivity were dependent on the type of reflecting surface. Limb brightening was reduced (darkening enhanced) over diffuse surfaces relative to specular surfaces.

Considerable emphasis was given the identification of spectral intervals at widely separated wavenumbers with the same general response to the cloud-free atmosphere. Although some very good matches were obtained, it is difficult to achieve a meaningful match unless both regions have the same distributions of absorber types. Without such similarity, a match found under one condition would not hold for another. For those interval pairs with responses from near the lower boundary, the spectral variation of the continuum attenuation causes a matching problem. When a match is

found, the spectral variation of the temperature sensitivity in the Planck function causes the higher wavenumbers to show higher temperatures over a nonhomogeneous scene. Different intervals with matching cloud-free responses will be useful for the identification of spectrally varying radiative properties of clouds, once proper physical cloud models are introduced. High priority should be given to the application of a suitable cloud model.

REFERENCES

1. P. Davis, "Atmospheric Transmittance Models for Infrared Radiometric Measurements," Final Report Contract 3-35208, SRI International, Menlo Park, California (March 1974).

2. R. A. McClatchey et al., "AFCRL Atmospheric Absorption Line Parameters Compilation," Environmental Research Papers No. 434, AFCRL-TR-0096, Air Force Cambridge Research Laboratories, L. G. Hanscom Field, Bedford, Massachusetts (January 1973).

3. J. F. Kielkopf, "New Approximation to the Voigt Function with Application to Spectral-line Profile Analysis," J. Opt. Soc. Am., 63, 987-995 (1973).

4. J.E.A. Selby, E. P. Shettle, R. A. McClatchey, "Atmospheric Transmittance from 0.25 to 28.5 μm: Supplement LOWTRAN 3B(1976)," AFGL-TR-76-0258, Optical Physics Division, Air Force Geophysics Laboratory, Hanscom AFB, Massachusetts (1976).

5. R. E. Roberts, J.E.A Selby, and L. M. Biberman, "Infrared Continuum Absorption by Atmospheric Water Vapor in the 8-12 μm Window," Appl. Opt., 15, 2085-2090 (1976).

6. P. W. Rosenkranz, "Shape of the 15 mm Oxygen Band in the Atmosphere," IEEE Trans. Antennas and Propagation, Vol. AP-23, 498-506 (1975).

7. D. H. Staelin, "Measurements and Interpretation of the Microwave Spectrum of the Terrestrial Atmosphere Near 1-Centimeter Wavelength," J. Geophys. Research, 71, 2875-2881 (1966).

8. N. E. Gaut and E. C. Reifenstein, III, "Interaction Model of Microwave Energy and Atmospheric Variables," Contractor Report NASA CR-61348, Environmental Research and Technology, Inc., Lexington, Massachusetts (1971).

9. W. Malkmus, "Random Lorenz Band Model with Exponential-Tailed S^{-1} Line-Intensity Distribution Function," J. Opt. Soc. Am., 57, 323-329 (1967).

10. R. M. Goody, "A Statistical Model for Water-Vapor Absorption," Quart. J. Roy. Meteor, Soc., 78, 165-169 (1952).

11. L. M. McMillin and H. E. Fleming, "Atmospheric Transmittance of an Absorbing Gas: A Computationally Fast and Accurate Transmittance Model for Absorbing Gases with Constant Mixing Ratios in Inhomogeneous Atmospheres," Appl. Opt., 15, 358-363 (1976).

12. J. H. Pierluissi, R. B. Gomez, and R. E. Bruce, "Transmittance Model for Absorbing Gases with Variable Mixing Ratios in Inhomogeneous Atmospheres," Appl. Opt., 16, 18. (1977).

13. H. E. Fleming and L. M. McMillin, "Atmospheric Transmittance of an Absorbing Gas. 2: A Computationally Fast and Accurate Transmittance Model for Slant Paths at Different Zenith Angles," Appl. Opt., 16, 1366-1370 (1977).

14. L. D. Kaplan, M. T. Chahine, J. Susskind, and J. E. Searl, "Spectral Band Passes for a High Precision Satellite Sounder," Appl. Opt., 16, 322-325 (1977).

15. T. G. Kyle and A. Goldman, "Atlas of Computed Infrared Atmospheric Absorption Spectra," NCAR Technical Note NCAR-TN/STR-112, National Center for Atmospheric Research, Boulder, Colorado (1975).

16. R. A. McClatchey, R. W. Fenn, J. E. A. Selby, F. E. Volz, and J. S. Garing, "Optical Properties of the Atmosphere (Third Edition)," AFCRL-72-0497, Environmental Research Papers No. 411, Air Force Cambridge Research Laboratories, L. G. Hanscom Field, Bedford, Massachusetts (1972).

17. N. C. Grody, "Remote Sensing of Atmospheric Water Content from Satellites Using Microwave Radiometry," IEEE Trans. Antennas and Propagation, Vol. AP-24, 155-162 (1976).

18. R. J. Curran, "Variation of Cloud Emissivity in the Infrared," Proceedings, Conference on Atmospheric Radiation, Am. Meteor. Soc., Fort Collins, Colorado, Aug. 7-9, 1972, 103-107 (1972).

19. W. L. Smith, H. M. Woolf, C. M. Hayden, and W. C. Shen, "Nimbus -5 Sounder Data Processing System, Part II--Results," NOAA Technical Memorandum NESS 71, Department of Commerce, Washington, D. C. (1975).

20. D. J. McCleese and L. S. Wilson, "Cloud Top Heights from Temperature Sounding Instruments," Quant. J. R. Met. Soc., 102, 781-790 (1976).

Appendix A

SUMMARY OF COMPUTER PROGRAMS

Program	Function
RDGOAT	Reads AFGL tape of absorption line parameters, extracts parameters for materials and wavenumber of interest. Computes ratios of Lorentz to Doppler lines, lists and stores data.
DAVISV	Generates extensive files of monochromatic absorption coefficients for specified absorbers, temperatures, pressures and spectral spacing. Stored on tapes.
COMBIN	Weights absorption coefficients for uniformly mixed gases with ratio of their mixing ratio to that for CO_2. Sums weighted coefficients within same spectral region and restores in single file.
VTRAN	Uses absorption coefficients from DAVISV or COMBIN in conjunction with specified absorber amounts to produce spectrally averaged transmittance (monochromatic transmittances convolved with any stipulated spectral response function). Lists and cardpunches final transmittances.
TAUFIT	Two routines that apply a nonlinear least squares curve-fitting routine to data from VTRAN. TAUFIT1 applied at single reference temperature; solves for all parameters. TAUFIT2 holds one parameter fixed and solves for the other parameters at all temperatures, and computes temperature scaling coefficients to complete model.
RADIANT	In application to arbitrary atmospheric structures, uses modeled transmittance representation with coefficients for recovery of transmittance from transmittance function. Parameters for computing continuum transmittance also are provided along with any other special information, such as slant path desired. Transmittance (including continuum) and weighting function profiles generated; radiances computed.

SUMMARY OF COMPUTER PROGRAMS (concluded)

Program	Function
ABSO2	O_2 (5 mm) microwave absorption coefficients, transmittances, weighting functions, brightness temperatures.
ABH2O	Same function but for H_2O in vicinity of either 22 GHz or 183 GHz. Modified version (GAMAC) provides a card deck of absorption coefficients for combination with O_2 coefficients.
MICROW	Combines O_2 and H_2O absorption coefficients to provide joint transmittances.
PLOTAB	Plots absorption coefficients.
TAUPLT	Plots data points and corresponding transmittance representation.

Appendix B

RECOVERY OF TRANSMITTANCE FROM THE TRANSMITTANCE FUNCTION

The transmittance function Ψ_c is defined by Eq. (12) in the text. To avoid table look-up and interpolation, a numerical routine, based on a Chebyshev polynomial expansion available in FORTRAN (IBM Scientific Subroutine Package), is introduced for rapid recovery. Seven coefficients of the Chebyshev polynomial expansion appeared to be sufficient to ensure at least three-place accuracy in τ for the worst case. A set of coefficients, along with a pair of scaling coefficients x_0 and x_1, are required for each value of parameter C. In practice the logarithm of the transmittance function is determined, so that the coefficients were computed to relate $\ell n(-\ell n\tau)$ to $\ell n\Psi_c$.

The transmittance function, specified either by Eq. (13) or Eq. (14), is determined from atmospheric data and a known parameter C. The recovery procedure begins by defining

$$E = 2(x_1 \ell n\Psi_c + x_0)$$

and setting $H_1=H_0=0.0$, initially. Then the quantities H_2 and H_0 are determined from the following computational loop from i=1 through i=N:

$$H_2 = H_1 \; ; \; H_1 = H_0$$

$$j = N + 1 - i$$

$$H_0 = EH_1 - H_2 + C(j)$$

where C(j) is the set of Chebyshev coefficients (j=1, 2, ..., N). After the nth run, the resultant H_2 and H_0 determine the quantity F

$$F \equiv \ell n(-\ell n\tau) = 0.5\left[C(1) - H_2 + H_0\right]$$

and $$\tau = \exp(-\exp F).$$

Two special cases arise. For the parameter C=0.0

$$\tau = \exp(-\Psi_0)$$

and for C=1.0

$$\tau = 1 - \text{erf}\ (\sqrt{\pi}\ \Psi/2)$$

Table B-1 lists all of the coefficients of the Chebyshev polynomial expansions and required scaling coefficients. These coefficients relate only to the transmittance function, not the atmospheric representation.

Table B-1

COEFFICIENTS FOR NUMERICAL RECOVERY OF TRANSMITTANCE FROM NATURAL LOGARITHM OF TRANSMITTANCE FUNCTION

C	C(1)	C(2)	C(3)	C(4)	C(5)	C(6)	C(7)	X_0	X_1
1.00	-3.06770	4.69014	.24358	.11686	.04131	.00899	-.00215	.76314	.23187
.90	-3.01170	4.72462	.20747	.09061	.02530	.00087	-.00605	.73100	.22765
.80	-2.96753	4.74914	.17409	.06980	.01448	-.00348	-.00659	.70422	.22414
.70	-2.93146	4.76706	.14388	.05326	.00735	-.00546	-.00581	.68136	.22114
.60	-2.90124	4.78040	.11671	.04004	.00281	-.00599	-.00462	.66148	.21854
.50	-2.87542	4.79047	.09226	.02942	.00010	-.00565	-.00341	.64394	.21624
.40	-2.85302	4.79813	.07017	.02084	-.00132	-.00482	-.00234	.62828	.21419
.30	-2.83335	4.80398	.05016	.01389	-.00180	-.00372	-.00147	.61416	.21234
.20	-2.81590	4.80847	.03194	.00825	-.00163	-.00249	-.00080	.60131	.21066
.10	-2.80028	4.81188	.01582	.00369	-.00098	-.00123	-.00032	.58955	.20912
-.10	-2.77342	4.81637	-.01408	-.00296	.00122	.00117	.00018	.56867	.20640
-.20	-2.76177	4.81776	-.02708	-.00531	.00260	.00227	.00025	.55933	.20518
-.30	-2.75109	4.81871	-.03915	-.00714	.00409	.00328	.00022	.55060	.20404
-.40	-2.74125	4.81932	-.05037	-.00855	.00565	.00420	.00012	.54241	.20297
-.50	-2.73217	4.81963	-.06083	-.00959	.00725	.00502	-.00004	.53471	.20196
-.60	-2.72374	4.81972	-.07061	-.01032	.00886	.00576	-.00025	.52743	.20101
-.70	-2.71591	4.81960	-.07978	-.01078	.01047	.00641	-.00050	.52055	.20012
-.80	-2.70860	4.81933	-.08838	-.01101	.01207	.00698	-.00077	.51402	.19927
-.90	-2.70176	4.81892	-.09648	-.01104	.01364	.00748	-.00107	.50781	.19846
-1.00	-2.69535	4.81840	-.10412	-.01090	.01519	.00790	-.00137	.50189	.19769
-1.10	-2.68932	4.81779	-.11134	-.01061	.01670	.00827	-.00169	.49624	.19695
-1.20	-2.68365	4.81710	-.11816	-.01020	.01817	.00857	-.00201	.49084	.19625
-1.30	-2.67830	4.81634	-.12463	-.00967	.01960	.00882	-.00234	.48566	.19558
-1.40	-2.67324	4.81553	-.13077	-.00905	.02099	.00902	-.00266	.48070	.19493
-1.50	-2.66845	4.81468	-.13660	-.00834	.02233	.00917	-.00298	.47592	.19431
-1.60	-2.66391	4.81378	-.14215	-.00756	.02363	.00928	-.00329	.47133	.19372
-1.70	-2.65960	4.81286	-.14743	-.00672	.02489	.00936	-.00360	.46691	.19314
-1.80	-2.65551	4.81191	-.15247	-.00582	.02611	.00940	-.00390	.46265	.19259
-1.90	-2.65161	4.81094	-.15729	-.00488	.02728	.00940	-.00420	.45853	.19206
-2.00	-2.64789	4.80995	-.16188	-.00389	.02842	.00938	-.00448	.45455	.19154
-2.10	-2.64434	4.80895	-.16628	-.00287	.02951	.00934	-.00476	.45070	.19104
-2.20	-2.64095	4.80794	-.17049	-.00182	.03056	.00926	-.00502	.44697	.19056
-2.30	-2.63771	4.80692	-.17453	-.00074	.03158	.00917	-.00528	.44336	.19009
-2.40	-2.63461	4.80590	-.17840	.00036	.03256	.00906	-.00553	.43985	.18964
-2.50	-2.63164	4.80488	-.18211	.00148	.03351	.00893	-.00576	.43645	.18920

APPENDIX C

ADDITIONAL WEIGHTING FUNCTION PROFILES COMPUTED FOR SELECTED OXYGEN AND WATER VAPOR MICROWAVE FREQUENCIES

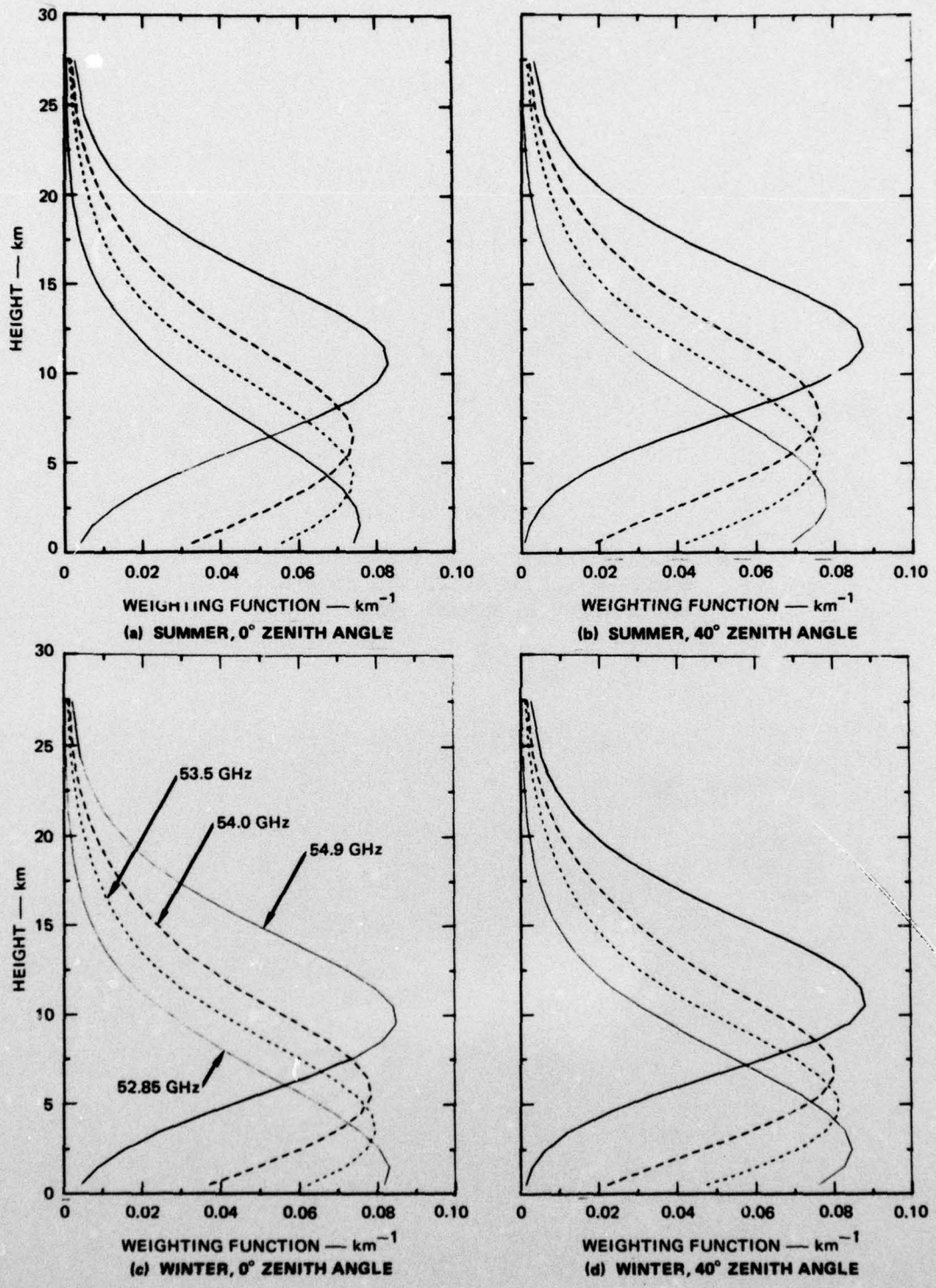

FIGURE C-1 OXYGEN TRANSMITTANCE WEIGHTING FUNCTIONS FOR 52.85, 53.5, 54.0, AND 54.9 GHz

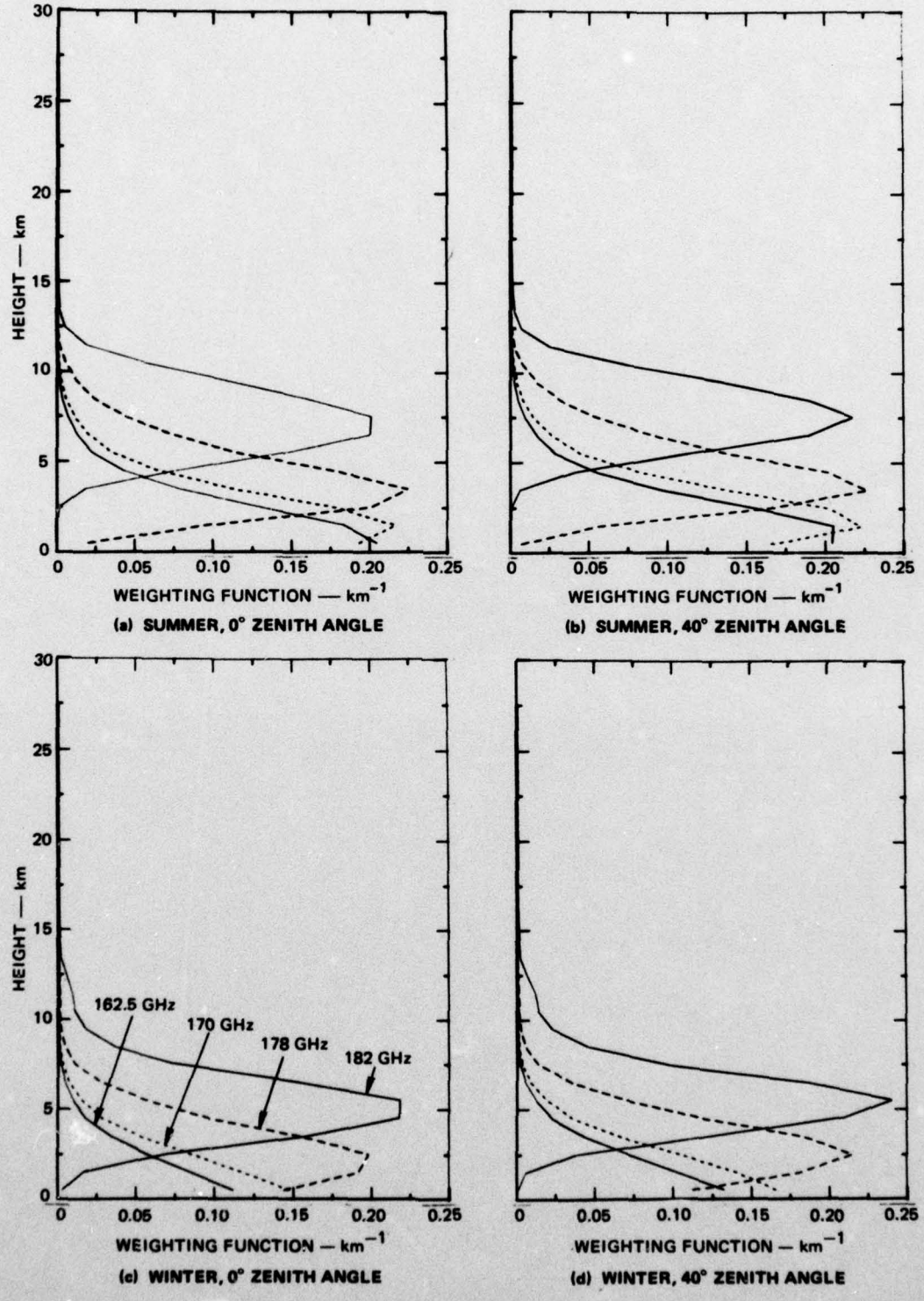

FIGURE C-2 WATER VAPOR TRANSMITTANCE WEIGHTING FUNCTIONS FOR 162.5, 170, 178, AND 182 GHz